

1 **Mechanistic investigations of the formation of highly oxidized**
2 **products from the multi-generation OH oxidation of styrene**

3 Long Chen,^{1,2,3} Yu Huang,^{*,1,2,3} Yonggang Xue,^{1,2,3} Long Cui,^{1,2,3,5} Zhihui Jia⁴

4 ¹ *State Key Laboratory of Loess Science, Institute of Earth Environment, Chinese*
5 *Academy of Sciences, Xi'an 710061, China*

6 ² *National Observation and Research Station of Regional Ecological Environment*
7 *Change and Comprehensive Management in the Guanzhong Plain, Xi'an 710061,*
8 *China*

9 ³ *Shaanxi Key Laboratory of Atmospheric and Haze-fog Pollution Prevention, Xi'an*
10 *710061, China*

11 ⁴ *School of Materials Science and Engineering, Shaanxi Normal University, Xi'an,*
12 *Shaanxi, 710119, China*

13 ⁵ *School of Environmental Science and Engineering, Hubei Key Laboratory of Mine*
14 *Environmental, Pollution Control and Remediation, Hubei Polytechnic University,*
15 *Huangshi 435003, China*

16

17

18 Submitted to *Atmospheric Chemistry & Physics*

19

20

21 *Corresponding author:

22 Prof. Yu Huang, E-mail address: huangyu@ieecas.cn

23

24 **Abstract**

25 Styrene is the second most efficient aromatic compound in the formation of
26 secondary organic aerosol (SOA) after toluene. Recent experiments have identified C₇
27 and C₈ series compounds as the main components of SOA in the photooxidation of
28 styrene. However, their molecular structures and formation pathways remain largely
29 uncharacterized. Herein, the formation mechanisms of highly oxidized products from
30 the multi-generation OH oxidation of styrene are studied using the quantum
31 chemistry methods. The calculations show that the addition of OH radicals to the
32 C_β-site of vinyl group is the dominant pathway, with benzaldehyde, 1st-ROOH
33 (C₈H₁₀O₃) and 1st-RONO₂ (C₈H₉NO₃) being the main closed-shell C₇- and
34 C₈-products in the first generation OH oxidation. For the second generation OH
35 oxidation, OH-addition reaction occurring at the C₁-site of 1st-ROOH and 1st-RONO₂
36 has a significant dominance. The resulting peroxide bicyclic peroxy radicals (BPR)
37 can react with HO₂ radicals and NO to form the closed-shell C₈-products 2nd-ROOH
38 (C₈H₁₂O₈) and 2nd-RONO₂ (C₈H₁₀N₂O₁₀), with the fractional yields of 41.4% and
39 4.8%. The peroxide bicyclic alkoxy radical (BAR) can proceed either the
40 ring-opening reactions to form the dicarbonyl C₄-species, or undergo the cyclization
41 reactions to generate the highly oxidized C₆-epoxides. For the third generation OH
42 oxidation, *syn*-OH-addition occurring at the C=C double bond of 2nd-ROOH and
43 2nd-RONO₂ has the smallest barrier. The major closed-shell C₈-products are the
44 multifunctional hydroperoxides and organic nitrates which possess a peroxide bridge,
45 two carbonyls, and two hydroxy. The volatility of the multi-generation OH oxidation
46 products significantly decreases with increasing the number of OH oxidation steps.

47

48 **1. Introduction**

49 Aromatic compounds are recognized as the significant secondary organic aerosol
50 (SOA) precursors, accounting for 20%-30% of the total volatile organic compounds
51 (VOCs) and up to ~60% of the urban atmosphere (Xu et al., 2020; Yan et al., 2019; Yu
52 et al., 2022; Cabrera-Perez et al., 2016; Iyer et al., 2023; Wang et al., 2017; Bloss et

53 al., 2005; Forstner et al., 1997). The primary sources include the incomplete
54 combustion, solvent evaporation, and industrial emission, and the secondary sources
55 involve the biofuel and biomass burning (Xu et al., 2020; Cabrera-Perez et al., 2016;
56 Li et al., 2019). The most abundant aromatic compounds, including benzene, toluene,
57 ethylbenzene, xylenes, styrene and trimethylbenzenes, are highly present in urban
58 environments (Cabrera-Perez et al., 2016; Koppmann, 2008). The degradation of
59 aromatic compounds initiated by the atmospheric oxidants (e.g., OH radicals, NO₃
60 radicals, O₃, and Cl atom) leads to the formation of the highly oxidized products (e.g.,
61 nitroaromatics, dicarbonyls, cresols, epoxides) (Ji et al., 2017; Wu et al., 2014; Fu et
62 al., 2023; Wang and Li, 2021; Wang et al., 2013; Zaytsev et al., 2019; Wang et al.,
63 2020), significantly contributing to new particle formation (NPF) and SOA formation
64 (up to 50% in eastern China) in the atmosphere (Wang et al., 2017; Wang et al., 2020;
65 Garmash et al., 2020; Molteni et al., 2018; Nie et al., 2022).

66 Styrene has been identified as the second most efficient aromatic compound in
67 the formation of SOA after toluene (Sun et al., 2006; Tajuelo et al., 2019a), which is
68 primarily emitted from the anthropogenic activities such as solvent usage and vehicle
69 exhaust (Cho et al., 2014; Wu et al., 2021). Styrene is detected at the ppb levels in
70 urban environments, with the mixing ratios of 0.06-4.50 ppb (Cho et al., 2014; Huang
71 et al., 2019), which has been classified as a hazardous air pollutant in the 1990 Clean
72 Air Act due to the potential mutagen and carcinogen (Environmental Protection
73 Agency (EPA), 1990). Therefore, it is very necessary to investigate the degradation
74 mechanisms of styrene under atmospheric conditions. In general, the atmospheric
75 oxidation of styrene initiated by OH radicals is anticipated to be the dominant daytime
76 sink, and the lifetime is estimated to be ~ 8 h under the conditions of typical OH
77 radicals concentrations ($[OH] = \sim 2 \times 10^6$ molecules cm⁻³) (Wu et al., 2021; Shen et
78 al., 2022). Due to the existence of highly reactive vinyl and aromatic groups,
79 OH-initiated oxidation of styrene mainly comprise two kinds of pathways:
80 H-abstraction and OH-addition, in which C_β-site OH-addition reaction is expected to
81 be the predominant pathway (Wu et al., 2021; Wang et al., 2015; Zhang et al., 2024).
82 The formed products can combine with an O₂ molecule leading to the first generation

83 peroxy radicals, which can further react with NO resulting in the formation of
84 benzaldehyde and formaldehyde. The barrier of the rate-limiting step is predicted to
85 be 28.4 kcal/mol (Wang et al., 2015), implying that benzaldehyde is unlikely to be the
86 sole primary product in the oxidation of styrene due to their higher barriers.
87 Additionally, carbonyl oxides, formed in the ozonolysis of styrene, serve as the chain
88 units participating in the formation of oligomers (Yu et al., 2022). The volatility of
89 oligomers decreases dramatically as the successive addition of carbonyl oxides
90 increases, eventually transforming into extremely low volatility organic compounds
91 (ELVOC) and directly participating in NPF.

92 Experimentally, Cho et al., investigated the kinetics of the reaction styrene
93 + OH at 240-340 K and 1-3 Torr using the mass spectrometry technique (Cho et al.,
94 2014). They found that the addition of OH radicals to the vinyl carbons is dominant,
95 and the determined rate coefficient is $(5.80 \pm 0.49) \times 10^{-11} \text{ cm}^3 \text{ molecule}^{-1} \text{ s}^{-1}$ at room
96 temperature. In the smog chamber experiments, Tajuelo et al., (2019a, 2019b and
97 2019c) found that the SOA yields from the photolysis and photooxidation of styrene
98 and its homologous species increase with the concentration of initial reactants
99 increasing, and benzaldehyde, benzoyl chloride, acetophenone and formaldehyde are
100 expected to be the primary gas phase products. Yu et al. (2022) investigated the
101 formation of SOA from styrene in an indoor chamber under different NO_x and RH
102 conditions, and found the SOA yields decrease with increasing RH in both the H₂O₂
103 and NO_x systems. The C₇ and C₈ species are the main products in the H₂O₂ system,
104 while organic nitrates are the major components in the NO_x system. Although the
105 possible molecular formula and chemical composition of the oxidation products from
106 the reaction styrene + OH are given in the aforementioned studies, the specific
107 molecular structures and formation pathways remain ambiguous. Additionally, to the
108 best of our knowledge, the majority of studies mainly focus on the first
109 generation OH oxidation products to date, while the formation mechanisms of highly
110 oxidized products from the multi-generation OH oxidation of styrene are still limited.

111 In the present study, the multi-generation OH oxidation mechanisms of styrene
112 in the presence of HO₂ /NO are investigated using the quantum chemistry methods.

113 The calculated results arising from the first generation OH oxidation reactions are
114 presented herein for comparison with the available literatures to ascertain the
115 reliability of the employed theoretical method. For the multi-generation OH
116 oxidation reactions of styrene, all the possible pathways, including H-abstraction,
117 OH-addition, O₂-addition, cyclization, ring-opening, intramolecular H-shifts, C-C
118 bond and O-O bond scission, and HO₂-elimination, are taken into account.
119 Additionally, the saturated concentrations of the formed highly oxidized products are
120 estimated to identify the volatility classes.

121 **2. Computational methods**

122 **2.1 Electronic structures and energy calculations**

123 The electronic structures and energy calculations of all stationary points,
124 including reactants (R), intermediates (IM), transition states (TS) and products (P), are
125 performed using the Gaussian 16 program (Frisch et al., 2016). Geometric
126 optimizations of all stationary points on the potential energy surfaces (PESs) are
127 carried out at the M06-2X/6-31+g(d,p) level of theory, since it has reliable
128 performance for describing the noncovalent interactions, thermochemical, and
129 kinetics (Zhao and Truhlar, 2008). Harmonic vibrational frequencies are determined at
130 the M06-2X/6-31+g(d,p) theoretical level to confirm the characteristics of all
131 stationary points (a local minimum or a saddle point). The zero-point vibrational
132 energy (ZPVE) is scaled by a factor of 0.967 (Alecú et al., 2010). Intrinsic reaction
133 coordinate (IRC) calculations are carried out to ascertain the connection of the given
134 TS between the designated local minima R and P (Fukui, 1981). Single point energy
135 calculations are performed at the M06-2X/6-311++G(3df,3pd) level based on the
136 M06-2X/6-31+g(d,p) optimized geometries.

137 In order to further evaluate the reliability of the computational method employed
138 herein, the single point energies of all the stationary points involved in the initial
139 addition of OH radicals to styrene and intramolecular H-shift reactions of the first
140 generation peroxy radicals S2-1-x are recalculated using the DLPNO-CCSD(T)/
141 aug-cc-pVTZ method performed using the Orca 6.1 program (Neese, 2025). As shown

142 in Table S1, the ΔE_a values obtained using the M06-2X/6-311++G(3df,3pd) method
143 are consistent with those derived from the DLPNO-CCSD(T)/aug-cc-pVTZ method.
144 The largest deviation and the average absolute deviation are 1.2 and 0.6 kcal/mol,
145 respectively, indicating that the computational method employed in this study is
146 reliable. Considering the computational cost, the M06-2X/6-311++G(3df,3pd) method
147 is employed to investigate the formation mechanism of highly oxidized products from
148 the multi-generation OH oxidation of styrene. The energy barrier (ΔE_a) and reaction
149 energy (ΔE_r) are defined as the difference in energy between TS and IM, as well as
150 between P and R.

151 **2.2 Conformer search**

152 RO₂ radicals formed from the addition of O₂ to the carbon-centered site of alkyl
153 radicals R have multiple possible conformers due to the different orientations of O₂
154 attack (Chen et al., 2021; Fu et al., 2020; Møller et al., 2016 and 2020). An initial
155 structure of RO₂ radicals is optimized at the B3LYP/6-31+G(d) level and
156 subsequently used as the starting geometry to perform the conformer search
157 conducted using the Molclus program (Lu, 2024). The resulting structures are initially
158 optimized at the B3LYP/6-31+G(d) level, as this method accurately predicts the
159 relative energy ordering of different conformers (Møller et al., 2016 and 2020). For
160 the intramolecular H-shift reactions of RO₂ radicals, the lengths of the O-O, C-H and
161 O-H bonds in the conformational sampling of TSs are constrained to retain the cyclic
162 TS structure. All unique conformers of R, TS and P within 5.0 kcal/mol with respect
163 to the lowest energy conformer are further optimized at the M06-2X/6-31+g(d,p) level
164 of theory. Then, the single point energy calculations are performed at the
165 M06-2X/6-311++G(3df,3pd) level of theory. RO radicals formed by the bimolecular
166 reactions of RO₂ radicals with HO₂ radicals and NO also have multiple conformers. In
167 order to obtain the lowest energy conformer, a similar methodology is employed in
168 the present study.

169 **2.3 Kinetics calculations**

170 The rate coefficients of unimolecular reactions, including intramolecular H-shifts,

171 cyclization, HO₂-elimination, and C-C bond and C-O bond scissions, are calculated
 172 using the RRKM theory along with energy-grained master equation (RRKM-ME)
 173 (Holbrook et al., 1996). The rate coefficients of bimolecular reactions, involving
 174 H-abstraction and OH-addition, are determined using the traditional transition state
 175 theory (TST) (Fernández-Ramos et al., 2007). An asymmetric one-dimensional Eckart
 176 model (Eckart, 1930) is employed to consider the tunneling correction factors in the
 177 rate coefficient calculations based on RRKM-ME and TST. A single exponential down
 178 model in the RRKM-ME calculations is utilized to approximate the collision transfer
 179 ($\langle \Delta E \rangle_{\text{down}} = 200 \text{ cm}^{-1}$). The Lennard-Jones parameters of all intermediate species are
 180 estimated using the empirical formula as proposed by Gilbert and Smith (1990).

181 For the intramolecular H-shifts of RO₂ and RO radicals, the rate coefficients are
 182 computed using the multiconformer transition state theory (MC-TST) (Møller et al.,
 183 2016), which is expressed as Eq. (1): (Møller et al., 2016 and 2020; Pasik et al., 2024)

$$184 \quad k_{\text{MC-TST}} = \kappa \frac{k_{\text{B}}T}{h} \frac{\sum_i^{\text{TS conf.}} \exp\left(\frac{-\Delta E_i}{k_{\text{B}}T}\right) Q_{\text{TS},i}}{\sum_j^{\text{R conf.}} \exp\left(\frac{-\Delta E_j}{k_{\text{B}}T}\right) Q_{\text{R},j}} \exp\left(-\frac{E_{\text{TS}} - E_{\text{R}}}{k_{\text{B}}T}\right) \quad (1)$$

185 where κ is the Eckart tunneling coefficient, h is Planck's constant, k_{B} is
 186 Boltzmann's constant, and T is the absolute temperature (298.15 K). $Q_{\text{TS},i}$ and $Q_{\text{R},j}$
 187 refer to the partition functions of the corresponding transition state i and reactant j
 188 conformers, respectively. ΔE_i and ΔE_j represent the relative electronic energies
 189 between the corresponding transition state i and reactant j conformers and the lowest
 190 energy conformers, respectively. E_{TS} and E_{R} stand for the electronic energies of the
 191 lowest energy transition state and reactant conformers, respectively. All kinetics
 192 calculations are carried out using the KiSThelP 2021 and MESMER 6.0 programs
 193 (Glowacki et al., 2012; Canneaux et al., 2013).

194 **3. Results and discussion**

195 **3.1 First generation OH oxidation mechanisms of styrene**

196 Styrene is composed of a benzene ring and a vinyl group, and its oxidation
 197 initiated by OH radicals may proceed either on the vinyl group or on the benzene ring.

198 Previous literature has demonstrated that the addition of OH radicals to terminal
199 carbon (C_{β} -site) of a vinyl group in styrene is the dominant pathway, with the
200 branching ratio of 88.2% (Wu et al., 2021). Therefore, the C_{β} -site OH-addition
201 reaction is mainly considered in the present study. Figure 1 depicts that this reaction
202 starts with the formation of a pre-reactive complex IM1, and then transforms into an
203 alkyl radical S1-1 via transition state TS1 with a ΔE_a of 0.8 kcal/mol. The rate
204 coefficient of C_{β} -site OH-addition reaction is estimated to be $1.5 \times 10^{-11} \text{ cm}^3$
205 $\text{molecule}^{-1} \text{ s}^{-1}$ at ambient temperature, which is approximately consistent with the
206 experimental ($1.2\text{-}6.2 \times 10^{-11} \text{ cm}^3 \text{ molecule}^{-1} \text{ s}^{-1}$) and theoretical values ($1.7\text{-}2.0 \times$
207 $10^{-11} \text{ cm}^3 \text{ molecule}^{-1} \text{ s}^{-1}$) for the total rate coefficient of the reaction styrene + OH
208 (Wu et al., 2021; Zhang et al., 2024).

209 Due to the existence of resonance structures with radical character on the
210 aromatic ring, the resulting S1-1 can readily isomerize into three other species,
211 namely, S1-2, S1-3 and S1-4. The attack of an O_2 molecule on the C-center site of
212 S1-1 leads to the formation of the first generation peroxy radicals S2-1-x ($\Delta E_r > -59.6$
213 kcal/mol). The formed S2-1-x includes eight energetically similar conformers due to
214 the different orientations of O_2 attack. In order to distinguish the different conformers,
215 the subscript letter x is used in the present study. The energy ordering of different
216 conformers follows an alphabetical sequence, in which letter a denotes the lowest
217 energy conformer. The Boltzmann population of different conformers in S2-1-x is
218 listed in Table S2.

219 For the unimolecular decomposition reactions of S2-1-x, there are three kinds of
220 pathways. One is the intramolecular H-shift reactions, where the hydrogen atom
221 migrates from the $-CH_2$, $-CH$ and $-OH$ groups to the terminal oxygen atom of the $-$
222 OO group leading to various alkyl and alkoxy radicals. Among these competing
223 H-shift reactions, the hydrogen atom at the $-OH$ group can be transferred via a
224 six-membered ring transition state (1,5-H shift) to yield an alkoxy radical S3-1-a,
225 which exhibits the lowest barrier ($\Delta E_a = 21.0$ kcal/mol). The resulting S3-1-a can
226 undergo the $C_{\alpha}\text{-}C_{\beta}$ bond cleavage to produce a formaldehyde and an alkyl radical
227 S4-1-a ($\Delta E_a = 0.8$ kcal/mol), followed by an OH radical release to form benzaldehyde

228 ($\Delta E_a = 0.1$ kcal/mol). The rate coefficients for the aforementioned three pathways are
229 calculated to be 2.7×10^{-4} , 4.6×10^{10} and 7.2×10^{10} s⁻¹, respectively. Based on the
230 values of ΔE_a and the corresponding rate coefficients, it can be concluded that the
231 1,5-H shift reaction is the rate-determining step in the formation of benzaldehyde. The
232 other is the cyclization, where the -OO group attacks the C=C double bond in the
233 benzene ring forming a cyclic peroxide alkyl radical S3-1-c ($\Delta E_a = 33.6$ kcal/mol).
234 The last is the HO₂-elimination, where a concerted process of C_α-O and C_β-H bonds
235 scission forms a closed-shell species S3-1-b and a HO₂ radical byproduct ($\Delta E_a = 33.3$
236 kcal/mol). The aforementioned results show that the cyclization and HO₂-elimination
237 reactions are less important due to their higher barriers.

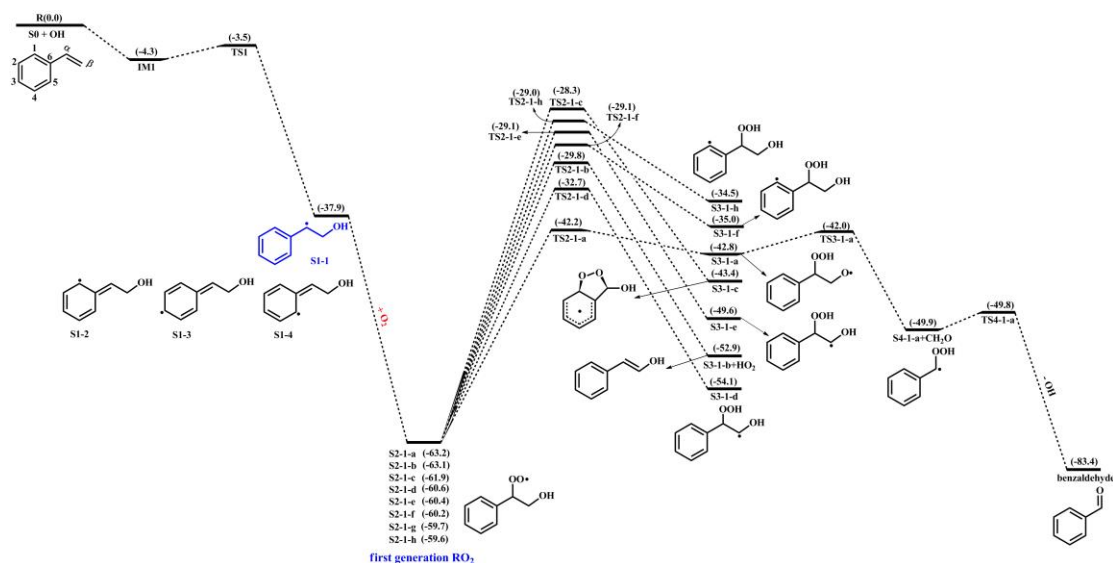
238 As depicted in Figure S1, the formations of the first generation peroxy radicals
239 S2-2-x from the association reaction S1-2 + O₂ are strongly endothermic ($\Delta E_r =$
240 8.1-10.4 kcal/mol), suggesting that they have a significant potential to redissociate
241 back to reactants S1-2 and O₂. The resulting S2-2-x can undergo through various
242 intramolecular H-shifts to yield distinct C-centered and O-centered radicals. Among
243 these competing H-shift pathways, hydrogen transfer from the -OH group to the
244 terminal oxygen of -OO group has the lowest barrier ($\Delta E_a = 17.4$ kcal/mol). A similar
245 conclusion is also obtained from the association reactions S1-3 + O₂ ($\Delta E_r = 6.6-7.1$
246 kcal/mol) and S1-4 + O₂ ($\Delta E_r = 8.1-11.1$ kcal/mol) that the formations of the first
247 generation peroxy radicals S2-3-x and S2-4-x are thermochemically unfavorable, and
248 their subsequent intramolecular H-shift barriers are considerably high (Figures S2 and
249 S3). Therefore, in the present study, we mainly focus on the subsequent reaction
250 mechanisms of S2-1-x under both low and high NO_x conditions.

251 In the low-NO_x conditions, the bimolecular reaction with HO₂ radicals is
252 expected to be the dominant sink for RO₂ radicals (Orlando and Tyndall, 2012;
253 Vereecken et al., 2015). Previous studies have reported that the rate coefficient
254 $k_{RO_2+HO_2}$ for the reactions of alkyl peroxy radicals with HO₂ radicals is 1.7×10^{-11}
255 cm³ molecule⁻¹ s⁻¹ (Atkinson and Arey, 2003; Boyd et al., 2003). The typical
256 atmospheric concentration of HO₂ radicals is 20-40 pptv (Wang et al., 2017; Bianchi
257 et al., 2019), resulting in the pseudo-first-order rate constant $k'_{RO_2+HO_2} = k_{RO_2+HO_2}$

258 [HO₂] of 0.01-0.02 s⁻¹. The isomerization reaction of RO₂ radicals is competitive with
259 the bimolecular reactions with HO₂ radicals only when the rate coefficient of
260 intramolecular H-shifts exceeds 0.01-0.02 s⁻¹. In the high-NO_x conditions, the
261 bimolecular reaction of RO₂ radicals with NO is considered to be a dominant sink
262 (Orlando and Tyndall, 2012; Vereecken et al., 2015). The rate coefficient $k_{\text{RO}_2+\text{NO}}$ for
263 the reaction of alkyl peroxy radicals with NO is determined to be $9.0 \times 10^{-12} \text{ cm}^3$
264 $\text{molecule}^{-1} \text{ s}^{-1}$ (Atkinson and Arey, 2003; Bianchi et al., 2019). The typical
265 atmospheric concentration of NO is 0.4-40 ppbv (Wang et al., 2017; Wang et al.,
266 2019), leading to the pseudo-first-order rate constant $k'_{\text{RO}_2+\text{NO}} = k_{\text{RO}_2+\text{NO}} [\text{NO}]$ of
267 0.1-10 s⁻¹. The intramolecular H-shift reaction of RO₂ radicals can compete with the
268 bimolecular reaction with NO only when the rate coefficient of the former case
269 exceeds 10 s⁻¹. Therefore, we use the $k'_{\text{RO}_2+\text{HO}_2}$ (0.01-0.02 s⁻¹) and $k'_{\text{RO}_2+\text{NO}}$ (0.1-10 s⁻¹)
270 values as thresholds to evaluate the relative importance of the isomerization reactions
271 of RO₂ radicals under the low- and high-NO_x conditions. Previous studies have also
272 employed the same methodology to evaluate the relative importance of isomerization
273 and bimolecular reactions of RO₂ radicals during the OH-initiated oxidation of
274 organophosphate esters and alkylbenzenes (Wang et al., 2017; Fu et al., 2024). For the
275 intramolecular H-shift reactions of S2-1-x, the rate coefficient $k_{\text{MC-TST}}$ is estimated to
276 be $1.6 \times 10^{-4} \text{ s}^{-1}$, which is 2-4 orders of magnitude lower than $k'_{\text{RO}_2+\text{HO}_2}$ and $k'_{\text{RO}_2+\text{NO}}$,
277 indicating that the isomerization reaction of S2-1-x is less competitive than the
278 bimolecular reactions with HO₂ radicals and NO.

279 In the presence of NO, the bimolecular reactions of S2-1-x with NO initially
280 proceed via oxygen-to-oxygen coupling to yield organic nitrites ROONO, which
281 subsequently decompose into benzaldehyde and CH₂OH radical or isomerize to
282 organic nitrates RONO₂. The energy barrier of the rate-limiting step predicted in
283 Wang's study for the formation of benzaldehyde is 28.4 kcal/mol, which is
284 approximately 4.0 kcal/mol greater than that for the formation of RONO₂ (Wang et al.,
285 2015). In the absence of NO, the hydroperoxides ROOH formed from the bimolecular
286 reaction of S2-1-x with HO₂ radicals are anticipated to be the dominate products. The
287 aforementioned results are further confirmed by the recent smog chamber experiment

288 study that C₇ and C₈ series products, as well as organic nitrates are the main
 289 components of SOA in the OH-initiated oxidation of styrene under different NO_x
 290 conditions (Yu et al., 2022). Considering that the extensive studies on the OH-initiated
 291 oxidation of benzaldehyde have done (Sebbar et al., 2011; Zhao et al., 2022; Iuga et
 292 al., 2008), this study primarily focuses on the multi-generation OH oxidation
 293 mechanisms of ROOH and RONO₂ under the low- and high-NO_x conditions.



294
 295 **Figure 1.** PES for the first-stage oxidation of styrene initiated by OH radicals and the
 296 isomerization reactions of S2-1-x at the M06-2X/6-311++G(3df,3pd)//M06-2X/6-31+g(d,p) level

297 3.2 Second generation OH oxidation mechanisms of 1st-ROOH 298 and 1st-RONO₂

299 The first generation products, including hydroperoxides 1st-ROOH and organic
 300 nitrates 1st-RONO₂, include multiple conformers. To obtain the global minimum of
 301 1st-ROOH and 1st-RONO₂, the conformer search is performed by using the Molclus
 302 program. The resulting structures are initially optimized at the M06-2X/6-31+g(d,p)
 303 level, then the single point energies are calculated at the M06-2X/6-311++G(3df,3pd)
 304 level. The global minimum structures of 1st-ROOH (S4) and 1st-RONO₂ (S5) are
 305 presented in Figure S4.

306 3.2.1 The oxidation mechanism of 1st-ROOH initiated by OH 307 radicals

308 The reaction 1st-ROOH (S4) + OH proceeds through the addition of OH radicals

309 to either side of the benzene ring to yield various alkyl radicals, as depicted in Figure
310 2. In the present study, *syn*-OH-addition is defined as the scenario in which the
311 addition of OH radicals occurs at the same side as the –OOH group, while
312 *anti*-OH-addition is referred to the scenario in which the addition of OH radicals
313 occurs at the opposite side as the –OOH group. For the *syn*-OH-addition reactions, the
314 addition of OH radicals to the C1-site of 1st-ROOH (S4) exhibits the lowest barrier
315 ($\Delta E_a = 3.6$ kcal/mol) due to the stability of the formed product, P_{S4-add1}'. A similar
316 conclusion is also obtained from the *anti*-OH-addition reactions that the OH-addition
317 pathway occurring at the C1-site is favorable ($\Delta E_a = 0.8$ kcal/mol). Notably, the
318 preferred OH-addition pathway in the *anti*-OH-addition reactions exhibits greater
319 competitiveness compared to that in the *syn*-OH-addition reactions. It can be
320 explained by the greater steric hindrance present in the latter reaction. In order to
321 further evaluate the reliability of our results, ΔE_a of all the *syn*-OH-addition and
322 *anti*-OH-addition reactions are recalculated using the DLPNO-CCSD(T)/
323 aug-cc-pVTZ//M06-2X/6-311+G(d,p) method. As shown in Table S3, the ΔE_a values
324 obtained using the M06-2X/6-311++G(3df,3pd) method are in good agreement with
325 those derived from the DLPNO-CCSD(T)/aug-cc-pVTZ method. The largest
326 deviation and the average absolute deviation are 1.2 and 0.9 kcal/mol, respectively,
327 indicating that the M06-2X/6-311++G(3df,3pd) method employed in this study is
328 reliable. Based on the values of ΔE_a obtained using the DLPNO-CCSD(T)/
329 aug-cc-pVTZ method, it can also be concluded that the addition of OH radicals to
330 C1-site, occurring at the opposite direction relative to the –OOH group, is
331 energetically favorable. The rate coefficients of the addition of OH radicals to the
332 different sites of 1st-ROOH are calculated to be 8.2×10^{-12} (C1-site), 5.8×10^{-15}
333 (C2-site), 8.3×10^{-15} (C3-site), 8.6×10^{-15} (C4-site), 2.7×10^{-12} (C5-site) and $4.1 \times$
334 10^{-13} (C6-site) cm³ molecule⁻¹ s⁻¹, respectively. The branching ratios for OH addition
335 to the C1, C5 and C6 sites are predicted to be 72.4%, 23.8% and 3.6%, respectively,
336 while the sum of branching ratios for OH addition to other carbon sites is less than
337 1%.

338 Our result is opposite to Zhang's finding that the addition of OH radicals to

339 C6-site would be the most favorable pathway (Zhang et al., 2024). The discrepancy
340 can be explained by the following three factors: (1) The 1st-ROOH conformer selected
341 in the Zhang's study is not the global minimum. In the present study, the global
342 minimum conformer of 1st-ROOH, identified through the conformer search, is found
343 to be 2.2 kcal/mol lower than the 1st-ROOH structure selected in the Zhang's study. (2)
344 The pre-reactive complexes are not considered in the Zhang's study. The addition of
345 OH radicals to C1-, C2-, C3- and C6-sites, occurring at the opposite direction relative
346 to the -OOH group, are merely considered in the Zhang's study. They found that the
347 apparent energy barrier of the addition of OH radicals to C6-site is smallest, and is
348 therefore expected to be the favorable pathway. Actually, these OH-addition reactions
349 are modulated by the pre-reactive complexes. It may be inappropriate to determine the
350 favorable pathway based solely on apparent activation energy without considering the
351 pre-reaction complexes. (3) From a geometric perspective, the addition of OH radicals
352 to C6-site is associated with greater steric hindrance compared to other sites, as
353 C6-atom connects with a larger functional group. Base on the aforementioned
354 discussions, we believe that the addition of OH radicals to C6-site is unlikely to be the
355 dominant pathway. Our calculations also confirm that the addition of OH radicals to
356 C6-site is less importance compared to that at the C1-site.

357 Our conclusion is further supported by the reaction toluene + OH that the
358 *ortho*-OH-addition reaction exhibits significant dominance, with the branching ratio
359 of up to 69.8-75.8% (Ji et al., 2017; Zhang 2019; Wu et al., 2020). Considering the
360 high reactivity of *ortho*-OH-addition in the reactions toluene + OH and 1st-ROOH
361 (S4) + OH, the substitute effects of the -CH₃ and -OOH groups are explicitly
362 discussed in the present study. Notably, the -CH₃ group in toluene is bonded to the C6
363 atom, and the -OOH group in 1st-ROOH is bonded to the C α atom, as depicted in
364 Figure S5. The optimized geometries of toluene and 1st-ROOH and the NPA atomic
365 charges of all the carbon atoms in the benzene ring are displayed in Figure S5. The
366 C-C bond lengths and the C-C-C bond angles in the benzene ring of toluene are
367 approximately 1.39 Å and 120°, respectively, which are consistent with those in the
368 benzene ring of 1st-ROOH. The aforementioned results show the effect of the -CH₃

369 and –OOH groups on the geometric structure of benzene ring is negligible. From the
370 perspective of NPA atomic charges, the charges on the C1 (-0.246 e) and C5 (-0.246 e)
371 atoms are more greater than those on the other carbon atoms in the benzene ring of
372 toluene. And the OH-adduct formed from the *ortho*-OH-addition reaction exhibits the
373 greater stability. These results indicate that the –CH₃ group is a typical *ortho*-directing
374 substituent and exerts an activating effect on the *ortho*-site of the benzene ring, which
375 explains why the *ortho*-OH-addition reaction is predominant in the reaction toluene
376 + OH. Compared with the charges on the carbon atoms in the benzene ring of toluene,
377 the charges on C1 and C6 atoms increase by 0.013 e and 0.057 e, respectively, in
378 1st-ROOH, which can be attributed to the electron-withdrawing effect of the –OOH
379 group. The charge on the C1 atom (-0.259 e) is the highest, and the stability of the
380 resulting OH-adduct is the greatest, implying that the addition of OH radicals to
381 C1-site is dominant in the reaction 1st-ROOH + OH. Therefore, a direct comparison
382 of the favorable OH-addition pathway in the reactions toluene + OH and 1st-ROOH
383 (S4) + OH is performed in this study.

384 The formed product P_{S4-add1} includes two conjugate double bonds (C₂=C₃ and
385 C₄=C₅), which can readily isomerize to P_{S4-add2} and P_{S4-add3}, as evident from Figure S6.
386 In the present of O₂, the attack of an O₂ molecule on the C-centered site of P_{S4-add1},
387 P_{S4-add2}, and P_{S4-add3} proceed via the barrierless processes to produce the second
388 generation peroxy radicals P_{S4-add1-a/-s}, P_{S4-add2-a/-s} and P_{S4-add3-a/-s}. The O₂-addition
389 reaction occurring at the same direction as the –OOH group is defined as
390 *syn*-O₂-addition, while the O₂-addition reaction occurring at the opposite direction as
391 the –OOH group is defined as *anti*-O₂-addition. For the reaction P_{S4-add1} + O₂ →
392 P_{S4-add1-a/-s}, ΔE_r of *anti*-O₂-addition is -5.8 kcal/mol, which is lower than that of
393 *syn*-O₂-addition by 0.4 kcal/mol, suggesting that *anti*-O₂-addition is preferable over
394 *syn*-O₂-addition in energy. For the reactions P_{S4-add2} + O₂ → P_{S4-add2-a/-s} and P_{S4-add3} +
395 O₂ → P_{S4-add3-a/-s}, it can be concluded the same by the ΔE_r values that
396 *anti*-O₂-addition reaction is energetically feasible.

397 The resulting P_{S4-add1-a/-s} can proceed intramolecular cyclization reaction, where
398 the attack of end-site oxygen atom of the –OO group on C2-site of the C₂=C₃ double

399 bond, leading to the formation of peroxide bicyclic alkyl radicals. ΔE_a and ΔE_r of the
400 reaction $P_{S4-add1-a} \rightarrow P_{S4-add1-a-1}$ are 11.8 and -16.8 kcal/mol, respectively, which are
401 lower than those of the reaction $P_{S4-add1-s} \rightarrow P_{S4-add1-s-1}$ by 3.9 and 2.2 kcal/mol,
402 respectively. The aforementioned results reveal that the intramolecular cyclization
403 reaction of *anti*-O₂-addition product $P_{S4-add1-a}$ is favorable on both thermochemically
404 and kinetically. A similar conclusion is also derived from the intramolecular
405 cyclization reactions of *anti*-O₂-addition products $P_{S4-add2-a}$ and $P_{S4-add3-a}$. Notably, the
406 barriers of the intramolecular cyclization reactions $P_{S4-add2-a} \rightarrow P_{S4-add2-a-1}$ ($\Delta E_a =$
407 31.1 kcal/mol) and $P_{S4-add2-a} \rightarrow P_{S4-add2-a-2}$ ($\Delta E_a = 34.6$ kcal/mol) are extremely high,
408 making them insignificant in the atmosphere. The tautomerization between
409 $P_{S4-add1-a-1}$ and $P_{S4-add3-a-1}$ readily occurs due to the existence of resonance structures,
410 and it is therefore that the latter conformer is selected as a prototype for the
411 investigating of its subsequent reaction mechanism.

412 The formed $P_{S4-add3-a-1}$ can combine with an O₂ molecule leading to the third
413 generation peroxy radicals (also called as peroxide bicyclic peroxy radicals, BPR)
414 $P_{S4-add3-a-2}$, and the lowest energy conformer is presented in Figure S7. The
415 isomerization of $P_{S4-add3-a-2}$ may undergo through a concerted process of the cleavage
416 of -O-O- bridge bond and C₁-C₂ bond as well as hydrogen atom transfer from the
417 hydroxyl group to the bridge oxygen atom, yielding a new peroxy radical ($\Delta E_a = 28.5$
418 kcal/mol). The room temperature rate coefficient is calculated to be $3.0 \times 10^{-9} \text{ s}^{-1}$,
419 which is several orders of magnitude low than the typical pseudo-first-order rate
420 constants $k'_{RO_2+HO_2}$ (0.01-0.02 s⁻¹) and k'_{RO_2+NO} (0.1-10 s⁻¹), suggesting that the
421 isomerization reaction is less importance in the atmosphere. Therefore, the
422 bimolecular reactions of $P_{S4-add3-a-2}$ with HO₂ radicals with NO are mainly taken into
423 consideration in this study.

424 In the pristine environments, $P_{S4-add3-a-2}$ can react with HO₂ radicals resulting in
425 the formation of the second generation products, bicyclic hydroperoxide 2nd-ROOH
426 (S6) and peroxide bicyclic alkoxy radical (BAR) $P_{S4-add3-a-3}$, as depicted in Figure S7.
427 For the subsequent reactions of S6 initiated by OH radicals, the detailed mechanisms
428 are discussed in Section 3.3.1. From Figure 3, it can be seen that the unimolecular

429 decomposition of P_{S4-add3-a-3} involves two kinds of pathways. One is the ring-opening
430 reaction, where the breakage of C₅-C₆ bond produces an alkyl radical S7 ($\Delta E_a = 5.9$
431 kcal/mol.). The other is cyclization reaction, where the attack of oxygen atom of
432 O-centered site on the C4-site of the C₃=C₄ double bond generates the ring-retaining
433 alkyl radical S15 ($E_a = 8.0$ kcal/mol). The branching ratios for the formation of S7 and
434 S15 are predicted to be 74.7% and 25.3%, respectively.

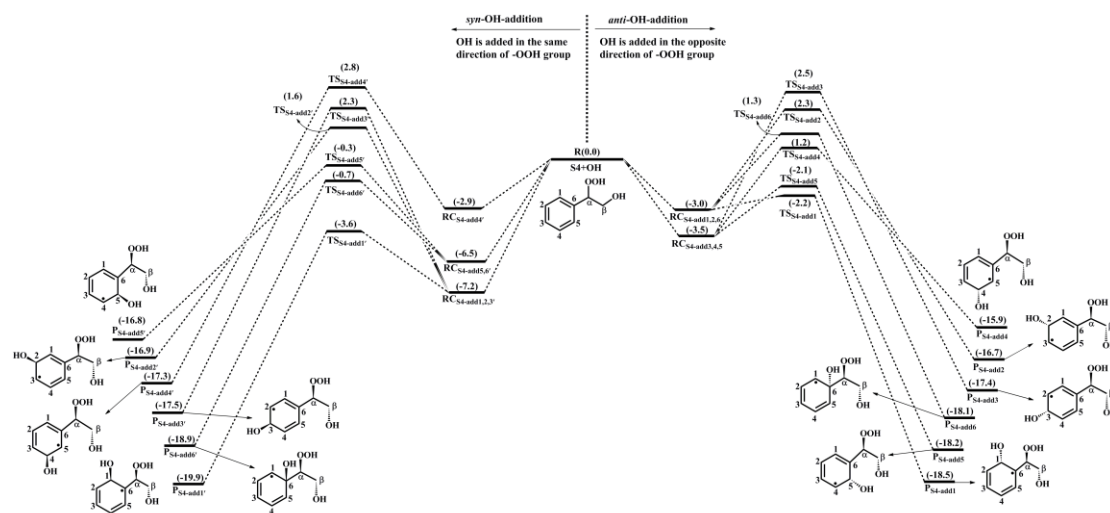
435 As shown in Figure 3, S7 decomposes through the barrierless rupture of -O-O-
436 bridge bond to form alkoxy radical S8-x, which includes five possible conformers as
437 presented in Figure S8. The Boltzmann populations of different conformers are listed
438 in Table S4. S8-x can undergo various intramolecular H-shifts, in which a hydrogen
439 atom is transferred from different carbon atoms to O-centered site, forming the alkyl
440 radicals. Among the competing H-shift reactions, 1,5 H-shift occurring at the -
441 C₅(O)H group exhibits the smallest barrier ($\Delta E_a = 0.6$ kcal/mol), and k_{MC-TST} is
442 calculated to be 8.2×10^9 s⁻¹ at ambient temperature (Table S5). The formed S8-c-P
443 can readily isomerize to S9 due to its resonance stabilized structure. The unimolecular
444 decomposition of S9 can proceed through the C1-C2 bond scission to produce a
445 ketene-enol S10 and an alkyl radical S10-1 ($\Delta E_a = 16.1$ kcal/mol), followed by
446 reaction with O₂ leading to a HO₂ radical and a 1,2-dicarbonyl compound S10-2 (ΔE_a
447 = 14.0 kcal/mol). Alternatively, S9 may undergo via the elimination of CO to generate
448 an alkyl radicals S11 ($\Delta E_a = 29.4$ kcal/mol). The aforementioned results show that the
449 formation of S10 and S10-1 is energetically favorable, with the rate coefficient k_{S10} of
450 26.1 s⁻¹.

451 In the presence of O₂, the attack of an O₂ molecule on the C-centered sites of S9
452 leads to the fourth generation peroxy radical S12-x ($\Delta E_r > -20.5$ kcal/mol). Adopting
453 the rate coefficient k_{R+O_2} of 6.0×10^{-12} cm³ molecule⁻¹ s⁻¹ for the reactions of alkyl
454 radicals with O₂, and the atmospheric O₂ concentration of 5×10^{18} molecule cm⁻³ (Ma
455 et al., 2021), the pseudo-first-order rate constant $k'_{R+O_2} = k_{R+O_2} [O_2]$ is 3.0×10^7 s⁻¹.
456 The unimolecular decomposition of alkyl radicals is competitive only when their
457 decay rate exceeds 3.0×10^7 s⁻¹. k'_{R+O_2} is about six orders of magnitude greater than
458 k_{S10} , indicating that the unimolecular decomposition of S9 is less importance. As

459 shown in Figure S9, S12-x can proceed various intramolecular H-shift reactions,
460 where hydrogen atom migrates from the different carbon sites or hydroxyl groups to
461 the terminal oxygen atom of the -OO group, resulting in the formation of QOOH
462 radicals and alkoxy radicals. Among these competing H-shift reactions, the 1,7-H
463 transfer at the C α -site leading to the formation of S12-d-P exhibits the smallest barrier
464 ($\Delta E_a = 17.4$ kcal/mol). Then, it decomposes to yield an OH radical and a closed-shell
465 product S13 containing a hydroperoxide, three hydroxyl and three carbonyl groups
466 ($\Delta E_a = 1.1$ kcal/mol).

467 S8-x can proceed through the C₁-C₂ bond scission to yield an unsaturated
468 1,4-dicarbonyl species S14 and an alkyl radical S10-1 ($\Delta E_a = 2.2$ kcal/mol), with the
469 rate coefficient of 2.1×10^{10} s⁻¹. Notably, both the 1,5 aldehyde H-shift and C₁-C₂
470 bond scission reactions yield a closed-shell species S10-2 with up to five oxygen
471 atoms, and the branching ratios are predicted to be 28.1% and 71.9%, respectively.
472 The result is further supported by the previous study that the proportion of aldehyde
473 H-shift products constitutes about one third of the total products in the reaction
474 benzene + OH (Wang et al., 2020).

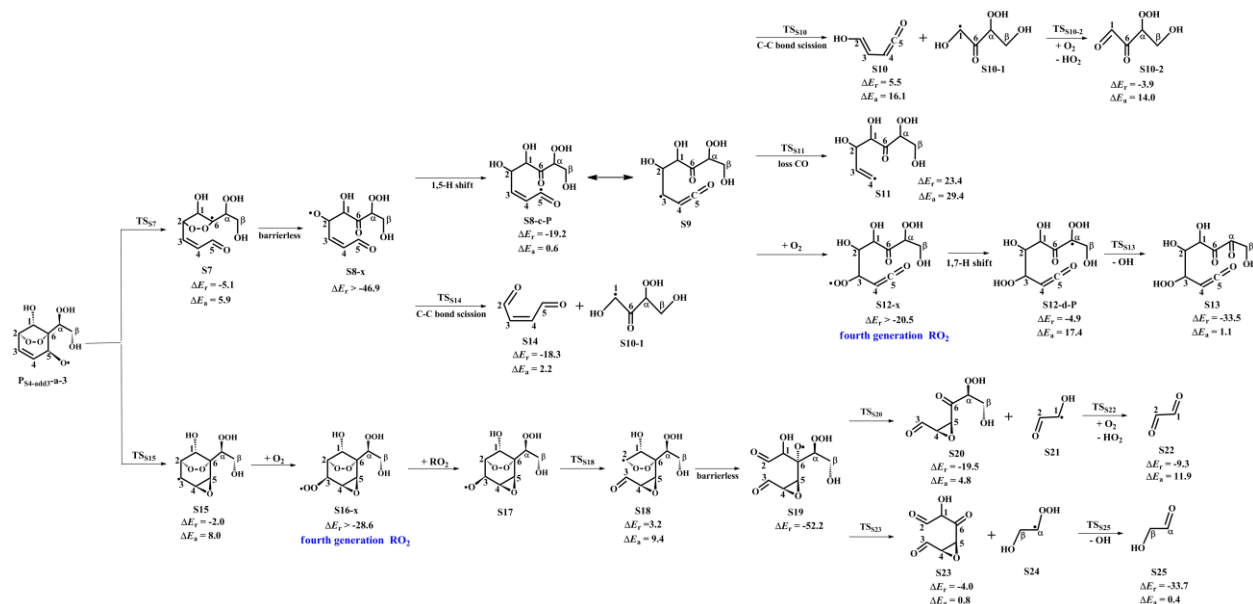
475 As shown in Figure 3, S15 can further react with O₂ leading to the fourth
476 generation peroxy radical S16-x, which can proceed either intramolecular H-shifts
477 forming QOOH radicals (Figure S10), or reactions with RO₂ radicals and NO forming
478 alkoxy radical S17. Notably, the barriers of intramolecular H-shifts are extremely
479 high ($\Delta E_a > 34.6$ kcal/mol), making them less importance in the atmosphere. The
480 transformation of S17 undergoes through the breakage of C₂-C₃ bond to produce an
481 alkyl radical S18 ($\Delta E_a = 9.4$ kcal/mol), followed by fragmentation into an alkoxy
482 radical S19 via the barrierless rupture of the -O-O- bridge bond. Then, S19 dissociates
483 to an OH radical, a glycolaldehyde S25 and a C₆-epoxide product S23 bearing a
484 hydroxy and three carbonyl groups, being the dominant pathway. The regeneration of
485 OH radicals drives the successive autoxidation of styrene, eventually leading to the
486 formation of the highly oxidized products.



487

488 **Figure 2.** PES for the oxidation of 1st-ROOH(S4) initiated by OH radicals at the
 489 M06-2X/6-311++G(3df,3pd)//M06-2X/6-31+g(d,p) level

490



491

492 **Figure 3.** PES for the unimolecular decomposition of P_{S4-add3-a-3} and its subsequent reactions at the
 493 M06-2X/6-311++G(3df,3pd)//M06-2X/6-31+g(d,p) level

494 **3.2.2 The oxidation mechanism of 1st-RONO₂ initiated by OH**
 495 **radicals**

496 The OH-initiated oxidation of 1st-RONO₂ (S5) proceeds through the addition of
 497 OH radicals to different carbon β sites in the benzene ring to form various alkyl radicals
 498 P_{S5-addx}, as depicted in Figure 4. Among the competing OH-addition reactions, the
 499 OH-addition reaction at the C1-site, which proceeds on the opposite direction as the –
 500 ONO₂ group, has the smallest barrier (R_{S5-add1}, ΔE_a = 0.4 kcal/mol) due to the stability

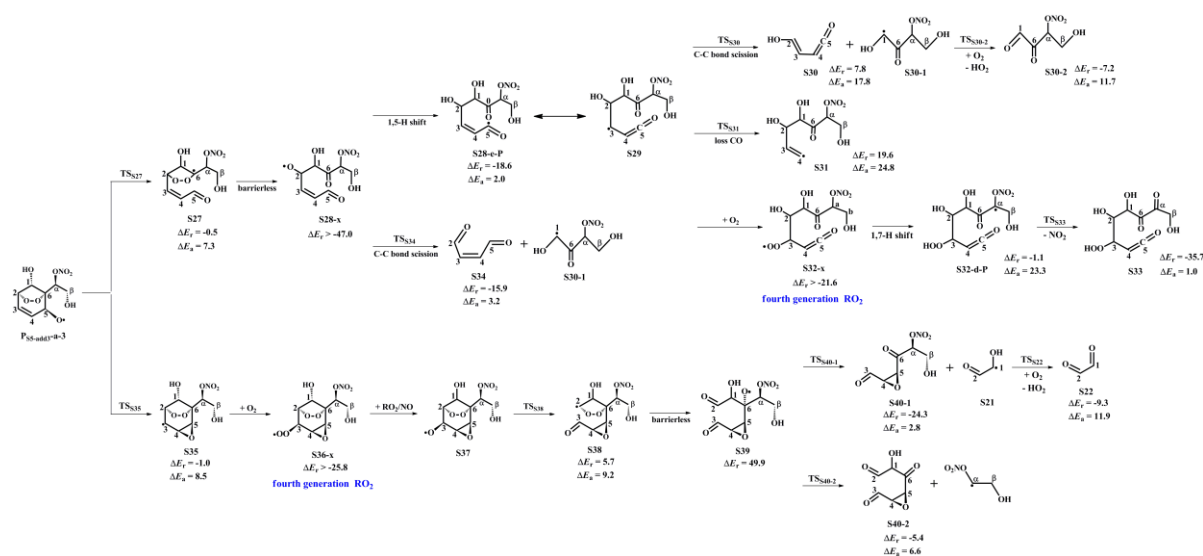
501 of the formed product $P_{S5-add1}$. The result again shows that the *ortho*-addition reaction
502 is energetically feasible. $P_{S5-add1}$ may isomerize to two other resonance structures,
503 namely, $P_{S5-add2}$ and $P_{S5-add3}$. For the reaction $P_{S5-add1} + O_2$, O_2 may add on either the
504 opposite (*anti*- O_2 -addition) or the same direction (*syn*- O_2 -addition) relative to the –
505 NO_3 group, leading to the second generation peroxy radicals $P_{S5-add1-a}$ and $P_{S5-add1-s}$
506 (Figure S11). The exoergicity of these two reactions are -6.7 and -4.4 kcal/mol,
507 respectively, suggesting that the *anti*- O_2 -addition reaction is thermochemically
508 favorable. Next, they can isomerize via a cyclization process to yield $P_{S5-add1-a-1}$ and
509 $P_{S5-add1-s-1}$ with the ΔE_a of 13.3 and 18.1 kcal/mol. This result shows that the
510 cyclization reaction of *anti*- O_2 -addition product $P_{S5-add1-a}$ is kinetically feasible. A
511 similar conclusion is also obtained from the reaction $P_{S5-add3} + O_2$ that the formation of
512 *anti*- O_2 -addition product $P_{S5-add3-a-1}$ is dominant. Due to the existence of the
513 conjugate double bond, it facilitates the tautomerization between $P_{S5-add1-a-1}$ and
514 $P_{S5-add3-a-1}$. Therefore, we mainly focus on the subsequent chemistry of $P_{S5-add3-a-1}$ in
515 the present study.

516 $P_{S5-add3-a-1}$ can further react with an O_2 molecule leading to the third generation
517 peroxy radicals $P_{S5-add3-a-2}$, which include multiple conformers. The lowest energy
518 conformer resulting from conformer search is presented in Figure S12. In urban
519 environments, the bimolecular reaction of $P_{S5-add3-a-2}$ with NO yields the second
520 generation products, a bicyclic organic nitrate 2nd-RONO₂ (S26) and a BAR
521 $P_{S5-add3-a-3}$, as displayed in Figure S12. The detailed mechanism of OH-initiated
522 oxidation of S26 is discussed in Section 3.3.2. As shown in Figure 5, $P_{S5-add3-a-3}$ can
523 either proceed via a ring opening process to form an alkyl radical S27 ($\Delta E_a = 7.3$
524 kcal/mol), or undergo through a cyclization process to generate an epoxide species
525 S35 ($\Delta E_a = 8.5$ kcal/mol). The branching ratios of these two reactions are predicted to
526 be 69.2% and 30.8%, respectively. Notably, the branching ratio of cyclization reaction
527 of $P_{S5-add3-a-3}$ increases by 5.5% compared to that of cyclization reaction of
528 $P_{S4-add3-a-3}$, suggesting that the $-ONO_2$ substitution is beneficial to cyclization
529 reaction.

530 The degradation of S27 proceeds through the barrierless scission of -O-O- bridge
531 bond to form S28-x, and the Boltzmann populations of different conformers are listed
532 in Table S6. S28-x can undergo via various intramolecular H-shifts to produce QOOH
533 radicals, in which hydrogen atom transfer from the -C(O)H group to the terminal
534 oxygen atom of the -OO group forming S28-e-P has the smallest barrier ($\Delta E_a = 2.0$
535 kcal/mol) (Figure S13). S28-e-P can readily isomerize to S29, which includes two
536 distinct decomposition pathways. One is the C1-C2 bond cleavage, yielding a
537 ketene-enol S30 and an alkyl radical S30-1 ($\Delta E_a = 17.8$ kcal/mol), followed by
538 reaction with O₂ to form a HO₂ radical and a 1,2-dicarbonyl species S30-2 ($\Delta E_a =$
539 11.7 kcal/mol). The other is the elimination of CO to generate an alkyl radical S31
540 ($\Delta E_a = 24.8$ kcal/mol), but the barrier is considerably high, making this pathway less
541 competitive. The rate coefficient for the formation of S30 and S30-1 is calculated to
542 be 14.4 s⁻¹, which is about six orders of magnitude lower than the pseudo-first-order
543 rate constant k'_{R+O_2} , indicating that the unimolecular decomposition of S29 is
544 insignificant.

545 In the presence of O₂, the bimolecular reaction of S29 with O₂ produces the
546 fourth generation peroxy radicals S32-x, comprising five energetically similar
547 conformers as shown in Figure S14. For the 1,7-H transfer reaction, hydrogen atom at
548 the C α -site can be transferred through an eight-membered ring transition state to
549 generate an alkyl radical S32-d-P ($\Delta E_a = 23.3$ kcal/mol), followed by the elimination
550 of NO₂ forming a closed product S33 ($\Delta E_a = 1.0$ kcal/mol). S33 and S13 are isomeric
551 species, with the former exhibiting more stability than the latter. S28-x can proceed
552 through the cleavage of C₁-C₂ bond to generate an unsaturated 1,4-dicarbonyl
553 compound S34 and an alkyl radical S30-1. The rate coefficients of the 1,5 aldehyde
554 H-shift and C1-C2 bond scission reactions are predicted to be 1.7×10^9 and 5.8×10^9
555 s⁻¹ (Table S7), respectively, with the branching ratios of 23% and 77%. S30-1, formed
556 from the above mentioned two pathways, may undergo through H-abstraction by O₂
557 to yield an organic nitrate S30-2 bearing a hydroxyl and two carbonyl groups ($\Delta E_a =$
558 11.7 kcal/mol).

559 S35 can combine with an O₂ molecule forming the fourth generation peroxy



578

579 **Figure 5.** PES for the unimolecular decomposition of P₅₅-add³-a-3 and its subsequent reactions at
 580 the M06-2X/6-311++G(3df,3pd)//M06-2X/6-31+g(d,p) level

581 3.3 Third generation OH oxidation mechanisms of 2nd-ROOH 582 and 2nd-RONO₂

583 The second generation products, bicyclic hydroperoxide 2nd-ROOH and bicyclic
 584 organic nitrate 2nd-RONO₂, have multiple possible conformers. The global minimum
 585 structures of 2nd-ROOH (S6) and 2nd-RONO₂ (S26) resulting from the conformer
 586 search are presented in Figures S7 and S12, respectively.

587 3.3.1 The oxidation mechanism of 2nd-ROOH initiated by OH 588 radicals

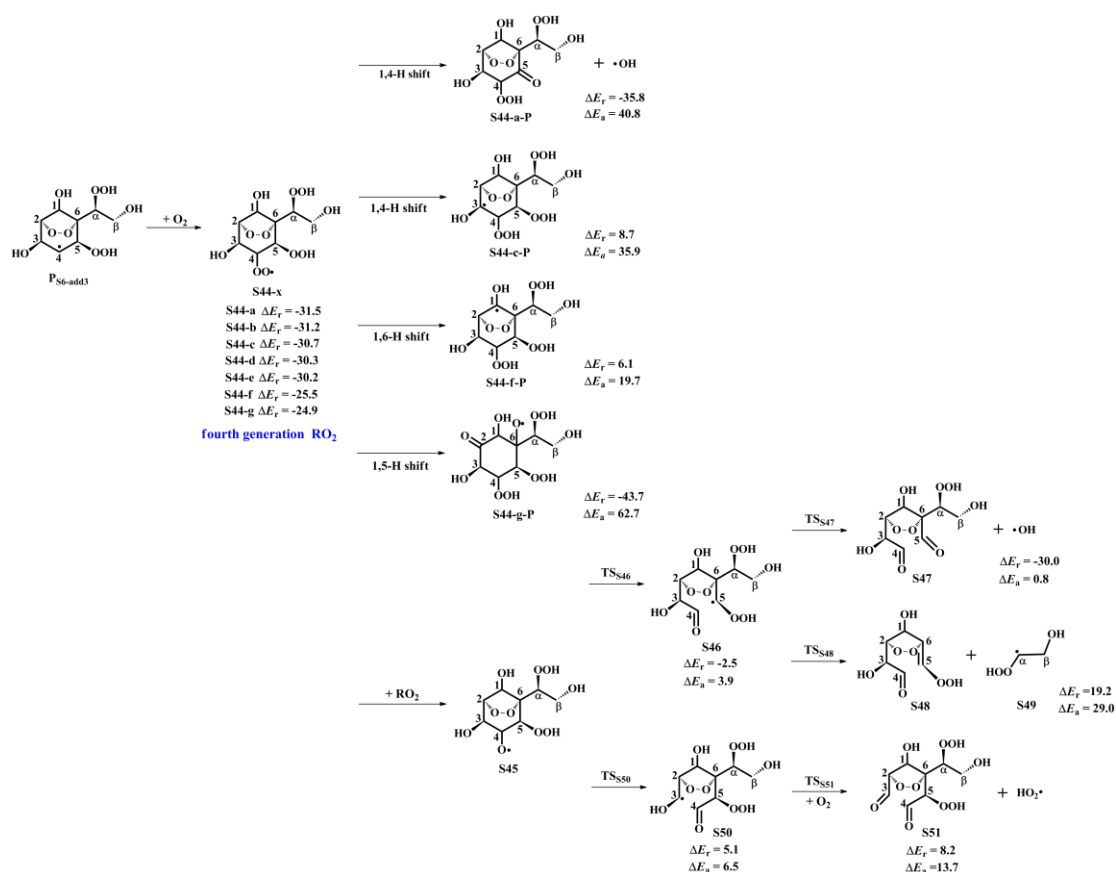
589 OH-initiated oxidation of 2nd-ROOH (S6) can either undergo through the
 590 addition of OH radicals to either side of the C₃=C₄ double bond to generate the alkyl
 591 radicals, or proceed via H-abstraction from the different carbon sites to produce the
 592 alkyl radicals and alkoxy radicals, as shown in Figures S16 and S17. For the
 593 OH-addition reactions, *syn*-OH-addition is defined as the addition of OH radicals on
 594 the same side as the -OOH group, while *anti*-OH-addition is referred to the addition
 595 of OH radicals on the opposite side as the -OOH group. The addition of OH radicals
 596 to the C3-site of the C₃=C₄ double bond forming the product P_{S6-abs3} has the smallest
 597 barrier (ΔE_a = 2.4 kcal/mol) and the exoergicity of -33.5 kcal/mol. For the
 598 H-abstraction reactions, the abstraction of hydrogen atom at the C5-site is the most

599 favorable pathway ($\Delta E_a = 3.6$ kcal/mol) and the exoergicity of -20.2 kcal/mol. It is
600 mainly because that the presence of an allyl group enhances the stability of the
601 resulting product $P_{S6-abs5}$. Notably, the abstraction of hydrogen atom at the C2-site
602 proceeds through a concerted process of C₂-H bond and -O-O- bridge bond rupture,
603 leading to the formation of an alkoxy radical $P_{S6-abs2}$ ($\Delta E_a = 7.2$ kcal/mol). This
604 reaction is expected to be less importance due to its higher energy barrier. The rate
605 coefficient of the favorable OH-addition reaction is calculated to be 6.4×10^{-11} cm³
606 molecule⁻¹ s⁻¹, which is about one order of magnitude greater than that of the
607 preferable H-abstraction reaction (4.1×10^{-12} cm³ molecule⁻¹ s⁻¹). Based on the above
608 discussion, it can be concluded that OH-addition reaction is favorable on both
609 thermochemically and kinetically. This conclusion is further supported by the OH +
610 alkene reaction systems that OH-addition pathways are predominant (Chen et al.,
611 2021; Yang et al., 2017; Arathala and Musah, 2024).

612 As depicted in Figure S18, the unimolecular decay of the product $P_{S6-add3}$
613 resulting from the favorable OH-addition reaction proceeds through a cyclization
614 process to yield an epoxide compound S41 and an OH radical byproduct with the ΔE_a
615 of 15.3 kcal/mol and the rate coefficient k_{R41} of 1.8×10^2 s⁻¹, or undergoes via
616 intramolecular 1,4 H-shift to form a peroxy radical S42 with the ΔE_a of 21.8 kcal/mol
617 and the rate coefficient k_{R43} of 1.9 s⁻¹, or proceeds via the elimination of hydrogen
618 atom to produce an alkene S43 with the ΔE_a of 37.9 kcal/mol. Based on the values of
619 ΔE_a and the corresponding rate coefficients, the dominant pathway of the
620 unimolecular decomposition of $P_{S6-add3}$ is the formation of S41. In the presence of O₂,
621 the pseudo-first-order rate constant k'_{R+O_2} of the reactions of alkyl radicals with O₂ is
622 3.0×10^7 s⁻¹, which is about five orders of magnitude greater than k_{R41} , suggesting
623 that the unimolecular decomposition of $P_{S6-add3}$ is insignificant.

624 As shown in Figure 6, the fourth generation peroxy radicals S44-x formed in the
625 addition reaction $P_{S6-add3} + O_2$ can either proceed via intramolecular H-shifts to form
626 QOOH, or undergo through self- or cross-reactions to yield an alkoxy radical S45.
627 Due to the considerably high barriers of intramolecular H-shifts, they are deemed to
628 be negligible under atmospheric conditions. S45 can convert into an alkyl radical S46

629 through the cleavage of C₄-C₅ bond, or dissociate to an alkyl radical S50 via the
 630 rupture of C₃-C₄ bond. The barrier of the former reaction is 3.9 kcal/mol, which is
 631 lower than that of the latter pathway by 2.6 kcal/mol, indicating that the formation of
 632 S46 is kinetically preferable. Then, S46 decomposes into an OH radical byproduct
 633 and a C₈-product S47 bearing a –OOH, a peroxide bridge, two carbonyls, and three
 634 hydroxy groups, which is expected to be the dominant pathway owing to its lower
 635 barrier. The rate coefficient k_{RS47} is estimated to be $1.8 \times 10^9 \text{ s}^{-1}$, which is about two
 636 orders of magnitude greater than the pseudo-first-order rate constant k'_{R+O_2} (3.0×10^7
 637 s^{-1}). The result reveals that the unimolecular decomposition of S46 is more
 638 competitive than the bimolecular reaction with O₂. The formed OH radicals can once
 639 again participate in the oxidations of styrene and its highly oxidized products,
 640 continuing these processes until they are completely consumed.



641
 642 **Figure 6.** PES for the subsequent reactions of P_{S6-add3} in the presence of O₂ at the
 643 M06-2X/6-311++G(3df,3pd)//M06-2X/6-31+g(d,p) level

644 **3.3.2 The oxidation mechanism of 2nd-RONO₂ initiated by OH**
 645 **radicals**

646 OH-initiated oxidation of 2nd-RONO₂ (S26) includes four different OH-addition
647 pathways and five different H-abstraction pathways, as displayed in Figures S19 and
648 S20. For the OH-addition reactions, the attack of OH radicals on the C3-site of the
649 C₃=C₄ double bond forming the product P_{S26-add3}, occurring on the same direction
650 relative to the -ONO₂ group, is found to be the favorable pathway ($\Delta E_a = 2.4$
651 kcal/mol, $\Delta E_r = -33.6$ kcal/mol). For the H-abstraction reactions, the abstraction of
652 hydrogen atom at the C5-site is identified as the preferable pathway ($\Delta E_a = 5.7$
653 kcal/mol, $\Delta E_r = -20.1$ kcal/mol) due to the enhanced stability of the resulting product
654 P_{S26-add5} by the presence of an allyl group. By comparing the values of ΔE_a and ΔE_r of
655 the favorable OH-addition and H-abstraction pathways, it can be concluded that the
656 former case is dominant on both thermochemically and kinetically. This conclusion is
657 consistent with the result from the reaction 2nd-ROOH (S6) + OH that OH-addition is
658 more competitive than H-abstraction.

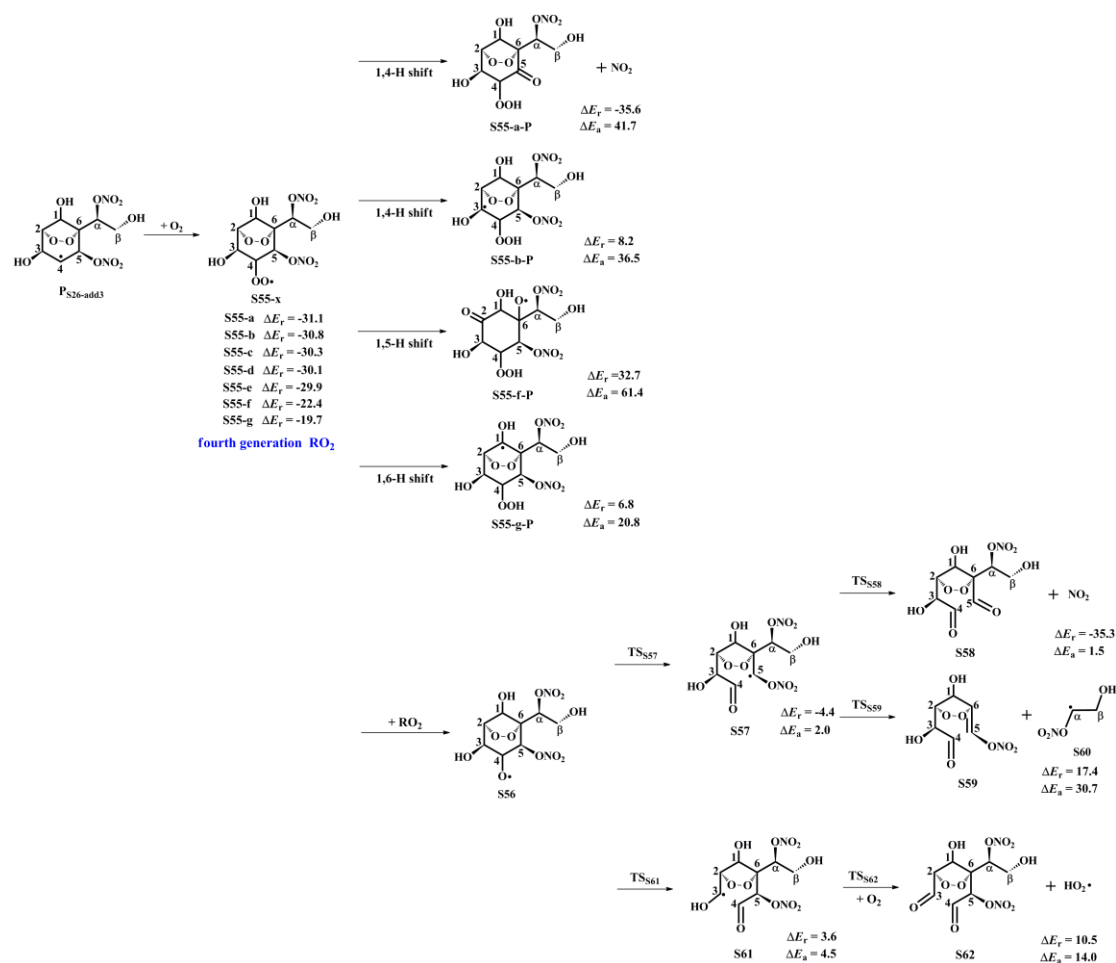
659 The product P_{S26-add3} arising from the favorable OH-addition pathway has three
660 potential unimolecular decay pathways, as depicted in Figure S21: (1) P_{S26-add3}
661 dissociates to an epoxide S52 and a NO₂ molecule through a cyclization process with
662 the ΔE_a of 18.5 kcal/mol and the rate coefficient k_{R52} of 0.4 s⁻¹; (2) P_{S26-add3} isomerizes
663 to an alkyl radical S53 via the intramolecular 1,2 H-shift ($\Delta E_a = 40.0$ kcal/mol); (3)
664 P_{S26-add3} converts into an alkene S54 via the elimination of hydrogen atom ($\Delta E_a = 39.1$
665 kcal/mol). Based on the value of ΔE_a and the corresponding rate coefficient, the
666 dominant pathway of the unimolecular decomposition of P_{S26-add3} is the formation of
667 S52. k_{R52} is about seven orders of magnitude lower than the pseudo-first-order rate
668 constant k'_{R+O_2} , indicating that the unimolecular decomposition of P_{S26-add3} is less
669 importance.

670 In the presence of O₂, P_{S26-add3} can react with an O₂ molecule leading to the
671 formation of the fourth generation peroxy radicals S55-x, comprising seven possible
672 conformers as shown in Figure 7. For the intramolecular H-shifts of S55-x, not all of
673 reactants (S55-c, S55-d and S55-e) have the suitable conformers that allow for the
674 pathways across the reaction barriers. The barriers of intramolecular H-shifts are
675 considerably high ($\Delta E_a = 20.8$ kcal/mol), making them uncompetitive in the

676 atmosphere. Alternatively, S55-x can react with other RO₂ radicals forming an alkoxy
677 radical S56, followed by decomposition into an alkyl radical S57 via the breakage of
678 C₄-C₅ bond ($\Delta E_a = 2.0$ kcal/mol), or fragmentation into an alkyl radical S61 through
679 the cleavage of C₃-C₄ bond ($\Delta E_a = 4.5$ kcal/mol). The aforementioned results reveal
680 that the formation of S57 is energetically favorable, which is consistent with the
681 conclusion derived from the unimolecular decomposition of S45 that the breakage of
682 C₄-C₅ bond is feasible. Next, S57 dissociates to a NO₂ coproduct and a C₈-product
683 S58 that possessed a -NO₃, a peroxide bridge, two carbonyls, and three hydroxy
684 groups. This pathway is expected to be the dominant one ($\Delta E_a = 1.5$ kcal/mol), with
685 the rate coefficient k_{RS58} of 1.2×10^9 s⁻¹. The resulting NO₂ can further participate in
686 the cycling of NO_x, ultimately generating tropospheric ozone and SOA.

687 The overall reaction mechanism and the fractional yields of the major products in
688 the multi-generation OH oxidation of styrene under different NO_x conditions are
689 presented in Figures S22 and S23. In the low-NO_x conditions, the fractional yield of
690 the first generation closed-shell product 1st-ROOH (S4) formed from the reaction
691 S2-1-x + HO₂ · is predicted to be 71.6%. For the second generation OH oxidation, the
692 reaction of the peroxy radical P_{S4-add3-a-2} with HO₂ radicals produces the second
693 generation closed-shell product 2nd-ROOH (S6) and an alkoxy radical P_{S4-add3-a-3},
694 with the fractional yields of 41.4% and 10.4%, respectively. The formed P_{S4-add3-a-2}
695 can either proceed through the C₅-C₆ bond scission to produce an alkyl radical S7 with
696 the fractional yield of 7.8%, or undergo via a cyclization process to generate an alkyl
697 radical S15 with the fractional yield of 2.6%. S7 and S15 can be transformed via a
698 series of reactions, ultimately leading to the formation of second generation
699 closed-shell product S10-2, S13 and S23, with the fractional yields of 5.6%, 2.2% and
700 1.3%, respectively. For the third generation OH oxidation, the degradation of
701 2nd-ROOH (S6) ultimately yields the third generation closed-shell products S47 and
702 S51, with the fractional yields of 26.3% and 0.3%, respectively. As a result, the major
703 closed-shell products are 1st-ROOH (S4), 2nd-ROOH (S6), S10-2, S13 and S47 in the
704 multi-generation OH oxidation of styrene in the low-NO_x conditions.

705 In the high-NO_x conditions, the fractional yield of the first generation
706 closed-shell product 1st-RONO₂ (S5) formed from the reaction S2-1-x + NO is
707 predicted to be 26.5%, as shown in Figure S23. As the OH oxidation reactions
708 proceed, 1st-RONO₂ (S5) can be initially transformed into the peroxy radical
709 P_{S5-add3-a-2}, followed by reaction with NO to form the second generation closed-shell
710 product 2nd-RONO₂ (S26) and an alkoxy radical P_{S5-add3-a-3}, with the fractional
711 yields of 4.8% and 11.2%, respectively. The decomposition of P_{S5-add3-a-3} undergoes
712 via two distinct pathways. One is the C₅-C₆ bond cleavage, leading to an alkyl radical
713 S27 with the fractional yield of 7.8%. The other is the cyclization, resulting in an
714 alkyl radical S35 with the fractional yield of 3.4%. The resulting S27 and S35
715 undergo multiple oxidation steps, finally leading to the formation of the second
716 generation closed-shell products S30-2, S33 and S40-1, with the fractional yields of
717 6.0%, 1.8%, and 1.7%, respectively. 2nd-RONO₂ (S26) can be further oxidized to
718 yield the third generation closed-shell products S58 and S62, with the fractional yields
719 of 2.6% and 0.03%, respectively. In summary, the major closed-shell products are
720 1st-RONO₂ (S5), 2nd-RONO₂ (S26), S30-2 and S58 in the multi-generation OH
721 oxidation of styrene in the high-NO_x conditions.



722

723 **Figure 7.** PES for the subsequent reactions of $\text{P}_{\text{S26-add3}}$ in the presence of O_2 at the
 724 M06-2X/6-311++G(3df,3pd)//M06-2X/6-31+g(d,p) level

725 3.4 Volatility Classes

726 The volatility classes for various organic compounds are based on their
 727 saturation concentration, as proposed by Donahue et al. (2012). The saturated vapour
 728 pressure (P^0) and saturated concentration (c^0) of styrene and its multi-generation OH
 729 oxidation products are predicted by using the SIMPOL.1 method (Pankow and Asher,
 730 2008). As show in Table S8, the P^0 and c^0 of the first generation closed-shell product
 731 benzaldehyde ($\text{C}_7\text{H}_6\text{O}$) are 7.62×10^{-4} atm and 2.89×10^6 ug/m³, respectively, which
 732 are 3-4 orders of magnitude greater than those of S4 ($\text{C}_8\text{H}_{10}\text{O}_3$, $P^0 = 1.43 \times 10^{-7}$ atm
 733 and $c^0 = 8.89 \times 10^2$ ug/m³) and S5 ($\text{C}_8\text{H}_9\text{NO}_3$, $P^0 = 2.54 \times 10^{-7}$ atm and $c^0 = 1.87 \times$
 734 10^3 ug/m³). Based on the values of c^0 , benzaldehyde is classified as the volatile
 735 organic compounds (VOCs), whereas S4 and S5 are classified as the intermediate
 736 volatility organic compounds (IVOCs). These first generation closed-shell products
 737 exist exclusively in the gas phase under atmospheric conditions (Bianchi et al., 2019).

738 For the second generation closed-shell products, S6 ($C_8H_{12}O_8$, $c^0 = 4.50 \times 10^{-2}$
739 ug/m^3) and S26 ($C_8H_{10}N_2O_{10}$, $c^0 = 0.18 ug/m^3$) formed from the bimolecular reactions
740 with HO_2 radicals and NO are classified as the low volatility organic compounds
741 (LVOCs). Similarly, S13 ($C_8H_{10}O_8$, $c^0 = 2.97 \times 10^{-2} ug/m^3$) and S33 ($C_8H_{10}O_8$, $c^0 =$
742 $2.97 \times 10^{-2} ug/m^3$), formed through the ring-opening and subsequent intramolecular
743 H-shift reactions of $P_{S4-add3-a-3}$ and $P_{S5-add3-a-3}$, respectively, are also classified as
744 LVOCs, which can condense onto the existing large particles (Bianchi et al., 2019).
745 The c^0 values of the remaining closed-shell products are significantly greater than
746 those of the aforementioned four products, for example, the c^0 values of S20 ($C_6H_8O_6$)
747 and S40-1 ($C_6H_7NO_7$), formed by the cyclization and decomposition reactions of
748 $P_{S4-add3-a-3}$ and $P_{S5-add3-a-3}$, are 42.21 and 75.86 ug/m^3 , respectively, classifying them
749 as the semivolatile organic compounds (SVOC).

750 For the third generation closed-shell products, the c^0 values of S47 ($C_8H_{12}O_9$, c^0
751 $= 2.68 \times 10^{-4} ug/m^3$) and S51 ($C_8H_{10}O_{10}$, $c^0 = 1.58 \times 10^{-4} ug/m^3$), formed through the
752 O_2 -addition and subsequent decomposition reactions of $P_{S6-add3}$, are about two orders
753 of magnitude lower than those of the second generation closed-shell products S6 and
754 S13, despite being classified as LVOCs. Similarly, S58 ($C_8H_{11}NO_{10}$, $c^0 = 5.37 \times 10^{-4}$
755 ug/m^3) and S62 ($C_8H_{10}N_2O_{12}$, $c^0 = 6.18 \times 10^{-4} ug/m^3$), formed via the O_2 -addition and
756 subsequent decomposition reactions of $P_{S26-add3}$, exhibit lower c^0 values compared to
757 the second generation closed-shell products S26 and S33. The aforementioned results
758 reveal that the volatility of the multi-generation OH oxidation products significantly
759 decreases with increasing the number of OH oxidation steps. As the oxidation
760 reactions of the third generation closed-shell products proceed further, the formed
761 products may possess sufficiently low volatility to participate in the formation and
762 growth of new aerosol particle.

763 **4 Conclusions**

764 The formation mechanisms of highly oxidized products from the
765 multi-generation OH oxidation of styrene under different NO_x conditions are

766 investigated by mean of quantum chemical methods. The primary conclusions are
767 summarized as follows.

768 (a) For the first generation OH oxidation of styrene, the addition of OH radicals
769 to terminal carbon (C_{β} -site) of a vinyl group is the dominant pathway. The
770 isomerization of the first generation RO_2 radicals, formed through the association
771 reaction of OH-adduct with O_2 , includes multiple intramolecular H-shift pathways
772 with the rate coefficient k_{MC-TST} of $1.6 \times 10^{-4} s^{-1}$. Among the competing H-shift
773 pathways, the hydrogen atom transfer from the $-OH$ group to the terminal oxygen
774 atom of the $-OO$ group has the lowest barrier. The resulting alkoxy radical
775 decomposes into benzaldehyde through the successive elimination of HCHO and an
776 OH radical. Alternatively, the first generation RO_2 radicals can proceed bimolecular
777 reactions with HO_2 radicals and NO, leading to the formation of the first generation
778 closed-shell products 1st-ROOH ($C_8H_{10}O_3$), benzaldehyde (C_7H_6O), and 1st-RONO₂
779 ($C_8H_9NO_3$).

780 (b) For the second generation OH oxidation of 1st-ROOH, the addition of OH
781 radicals to C_1 -site, occurring at the opposite direction relative to the $-OOH$ group, has
782 the smallest barrier. BPR formed by two O_2 -addition steps and a cyclization process
783 can either react with RO_2 radicals to produce BAR, or interact with HO_2 radicals to
784 form the second generation closed-shell product 2nd-ROOH ($C_8H_{12}O_8$). The resulting
785 BAR may undergo via the ring-opening and subsequent decomposition reactions to
786 generate an unsaturated 1,4-dicarbonyl compound S14 ($C_4H_4O_2$), a 1,2-dicarbonyl
787 species S10-2 ($C_4H_6O_5$) and a multifunctional compound S13 ($C_8H_{10}O_8$).
788 Alternatively, it can proceed through the cyclization and subsequent dissociation
789 reactions to produce a glycolaldehyde and a epoxide S23 ($C_6H_6O_5$) containing a
790 hydroxy and three carbonyl groups. The branching ratios of these two pathways are
791 74.7% and 25.3%, respectively.

792 (c) For the second generation OH oxidation of 1st-RONO₂, the OH-addition
793 reaction at the C_1 -site, occurring at the opposite direction as the $-ONO_2$ group, has
794 the smallest barrier. BPR can react with NO to form BAR and the second generation
795 closed-shell product 2nd-RONO₂ ($C_8H_{10}N_2O_{10}$). The resulting BAR can proceed either

796 the ring opening or cyclization process to yield alkyl radicals S27 and S35, with the
797 branching ratio of 69.2% and 30.8%. The main products of the decomposition of S27
798 are an unsaturated 1,4-dicarbonyl compound S34 ($C_4H_4O_2$), a multifunctional organic
799 nitrate S30-2 ($C_4H_5NO_6$) and a multifunctional compound S33 ($C_8H_{10}O_8$). The
800 primary products of the dissociation of S35 are a glyoxal and a C_6 -epoxide specie
801 S40-1 ($C_6H_7NO_7$) containing a $-NO_3$, a hydroxy and two carbonyl groups.

802 (d) For the third generation OH oxidation of 2nd-ROOH and 2nd-RONO₂,
803 *syn*-OH-addition reactions occurring at the C_3 -site are predominant. The alkoxy
804 radical formed in the reaction 2nd-ROOH + OH decomposes into an OH radical
805 byproduct and a C_8 -product ($C_8H_{12}O_9$) bearing a $-OOH$, a peroxide bridge, two
806 carbonyls, and three hydroxy groups. The alkoxy radical formed in the reaction
807 2nd-RONO₂ + OH dissociates to a NO₂ co-product and a C_8 -product ($C_8H_{11}NO_{10}$)
808 containing a $-NO_3$, a peroxide bridge, two carbonyls, and three hydroxy groups.

809 (e) In the low-NO_x conditions, the major closed-shell products formed from the
810 multi-generation OH oxidation of styrene are 1st-ROOH (S4), 2nd-ROOH (S6), S10-2,
811 S13 and S47, with the fractional yields of 71.6%, 41.4%, 5.6%, 2.2% and 26.3%,
812 respectively. In the high-NO_x conditions, the major closed-shell products are
813 1st-RONO₂ (S5), 2nd-RONO₂ (S26), S30-2 and S58, with the fractional yields of
814 26.5%, 4.8%, 6.0% and 2.6%, respectively.

815 (f) The first generation closed-shell products 1st-ROOH ($C_8H_{10}O_3$) and
816 1st-RONO₂ ($C_8H_9NO_3$) are classified as IVOCs, which exist exclusively in the gas
817 phase in the atmosphere. The second generation closed-shell products, S6 ($C_8H_{12}O_8$),
818 S26 ($C_8H_{10}N_2O_{10}$), S13 ($C_8H_{10}O_8$) and S33 ($C_8H_{10}O_8$) are classified as LVOCs, which
819 can condense onto the existing large particles. The third generation closed-shell
820 products S47 ($C_8H_{12}O_9$), S51 ($C_8H_{10}O_{10}$), S58 ($C_8H_{11}NO_{10}$) and S62 ($C_8H_{10}N_2O_{10}$)
821 exhibit lower c^0 values compared to the second generation closed-shell products,
822 despite being classified as LVOCs. As a result, the volatility of the
823 multi-generation OH oxidation products significantly decreases with increasing the
824 number of OH oxidation steps.

825

826 **Data availability**

827 The data are accessible by contacting the corresponding author
828 (huangyu@ieecas.cn).

829

830 **Supplement**

831 Tables S1 and S3 list the energy barriers of all the elementary reactions involved
832 in the addition of OH radicals to styrene and 1st-ROOH (S4) predicted at different
833 levels. Tables S2, S4 and S6 list the relative electronic energy, free energy and
834 Boltzmann population of different conformers involved in S2-1-x, S8-x and S28-x.
835 Tables S5 and S7 list the MC-TST rate coefficients for the intramolecular H-shift
836 reactions of S8-x and S28-x. Table S8 summaries the saturated vapour pressure and
837 saturated concentrations of styrene and its multiple generation OH oxidation
838 closed-shell products. Figures S1-S3 display the PESs for the unimolecular reactions
839 of S2-2-x, S2-3-x and S2-4-x. Figure S4 shows the global minimum structures of
840 1st-ROOH(S4) and 1st-RONO₂(S5). Figure S5 depicts the geometric parameters of
841 toluene and 1st-ROOH (S4) and the NPA atomic charges of all the carbon atoms.
842 Figures S6 and S11 show the PESs for the addition reactions P_{S4-add1} + O₂ and P_{S5-add1}
843 + O₂. Figures S7 and S12 present the lowest energy conformers of third generation
844 peroxy radicals P_{S4-add3-a-2} and P_{S5-add3-a-2}. Figures S8-S10 depict the PESs for the
845 intramolecular hydrogen transfer reactions of S8-x, S12-x and S16-x. Figures
846 S13-S15 depict the PESs for the intramolecular hydrogen transfer reactions of S28-x,
847 S32-x and S36-x. Figures S16-18 show the PESs for the OH-initiated oxidation of
848 2nd-ROOH (S6) and unimolecular decomposition of P_{S6-add3}. Figures S19-S21 show
849 the PESs for the OH-initiated oxidation of 2nd-RONO₂ (S26) and unimolecular
850 decomposition of P_{S26-add3}. Figures S22 and S23 show the overall reaction mechanism
851 of the multi-generation OH oxidation of styrene in the low- and high-NO_x conditions.

852

853 **Author contribution**

854 LC and YH conceptualized the study. LC conducted quantum chemical

855 calculation. YX and ZJ analyzed the data. LC conducted the volatility estimation. All
856 authors discussed the results and commented on the manuscript.

857

858 **Competing interests**

859 The contact author has declared that none of the authors has any competing interests.

860

861 **Financial support**

862 This study was supported by the National Natural Science Foundation of China (grant
863 nos. 42175134) and the Youth Innovation Promotion Association of the Chinese
864 Academy of Sciences (grant number 2022415).

865

866 **Reference**

- 867 Alecu, I. M., Zheng, J., Zhao, Y., and Truhlar, D. G.: Computational thermochemistry: scale factor
868 databases and scale factors for vibrational frequencies obtained from electronic model
869 chemistries, *J. Chem. Theory Comput.*, 6, 2872-2887, <https://doi.org/10.1021/ct100326h>,
870 2010.
- 871 Arathala, P., and Musah, R. A.: Atmospheric chemistry of chloroprene initiated by OH radicals:
872 combined Ab initio/DFT calculations and kinetics analysis, *J. Phys. Chem. A*, 128,
873 8983-8995, <https://doi.org/10.1021/acs.jpca.4c05428>, 2024.
- 874 Atkinson, R., and Arey, J.: Atmospheric degradation of volatile organic compounds, *Chem. Rev.*,
875 103, 4605-4638, <https://doi.org/10.1021/cr0206420>, 2003.
- 876 Bianchi, F., Kurt n, T., Riva, M., Mohr, C., Rissanen, M. P., Roldin, P., Berndt, T., Crouse, J. D.,
877 Wennberg, P. O., Mentel, T. F., Wildt, J., Junninen, H., Jokinen, T., Kulmala, M., Worsnop, D.
878 R., Thornton, J. A., Donahue, N., Kjaergaard, H. G., and Ehn, M.: Highly oxygenated organic
879 molecules (HOM) from gas-phase autoxidation involving peroxy radicals: a key contributor
880 to atmospheric aerosol, *Chem. Rev.*, 119, 3472-3509,
881 <https://doi.org/10.1021/acs.chemrev.8b00395>, 2019.
- 882 Bloss, C., Wagner, V., Jenkin, M. E., Volkamer, R., Bloss, W. J., Lee, J. D., Heard, D. E., Wirtz, K.,
883 Martin-Reviejo, M., Rea, G., Wenger, J. C., and Pilling, M. J.: Development of a detailed
884 chemical mechanism (MCMv3.1) for the atmospheric oxidation of aromatic hydrocarbons,
885 *Atmos. Chem. Phys.*, 5, 641-664, <https://doi.org/10.5194/acp-5-641-2005>, 2005.
- 886 Boyd, A. A., Flaud, P. M., Daugey, N., and Lesclaux, R.: Rate constants for RO₂ + HO₂ reactions
887 measured under a large excess of HO₂, *J. Phys. Chem. A*, 107, 818-821,
888 <https://doi.org/10.1021/jp026581r>, 2003.
- 889 Cabrera-Perez, D., Taraborrelli, D., Sander, R., and Pozzer, A.: Global atmospheric budget of
890 simple monocyclic aromatic compounds, *Atmos. Chem. Phys.*, 16, 6931-6947,
891 <https://doi.org/10.5194/acp-16-6931-2016>, 2016.

892 Canneaux, S., Bohr, F., and Henon, E.: KiSTheIP: a program to predict thermodynamic properties
893 and rate constants from quantum chemistry results, *J. Comput. Chem.*, 35, 82-93,
894 <https://doi.org/10.1002/jcc.23470>, 2013.

895 Chen, L., Huang, Y., Xue, Y., Jia, Z., and Wang, W.: Atmospheric oxidation of 1-butene initiated
896 by OH radical: Implications for ozone and nitrous acid formations, *Atmos. Environ.*, 244,
897 118010-118021, <https://doi.org/10.1016/j.atmosenv.2020.118010>, 2021.

898 Cho, J., Roueintan, M., and Li, Z.: Kinetic and dynamic investigations of OH reaction with
899 styrene, *J. Phys. Chem. A*, 118, 9460-9470, <https://doi.org/10.1021/jp501380j>, 2014.

900 Donahue, N. M., Kroll, J. H., Pandis, S. N., and Robinson, A. L.: A two-dimensional volatility
901 basis set – Part 2: Diagnostics of organic-aerosol evolution, *Atmos. Chem. Phys.*, 12,
902 615-634, <https://doi.org/10.5194/acp-12-615-2012>, 2012.

903 Eckart, C.: The penetration of a potential barrier by electrons, *Phys. Rev.*, 35, 1303-1309,
904 <https://doi.org/10.1103/PhysRev.35.1303>, 1930.

905 Environmental Protection Agency (EPA). Clean Air Act: Title I-Air Pollution Prevention and
906 Control. U.S. 1990.

907 Fernández-Ramos, A., Ellingson, B. A., Meana-Pañeda, R., Marques, J. M. C., and Truhlar, D. G.:
908 Symmetry numbers and chemical reaction rates, *Theor. Chem. Acc.*, 118, 813-826,
909 <https://doi.org/10.1007/s00214-007-0328-0>, 2007.

910 Forstner, H. J. L., Flagan, R. C., and Seinfeld, J. H.: Secondary organic aerosol from the
911 photooxidation of aromatic hydrocarbons: molecular composition, *Environ. Sci. Technol.*, 31,
912 1345-1358, <https://doi.org/10.1021/es9605376>, 1997.

913 Frisch, M. J., Trucks, G. W., Schlegel, H. B., Scuseria, G. E., Robb, M. A., Cheeseman, J. R.,
914 Scalmani, G., Barone, V., Petersson, G. A., Nakatsuji, H., Li, X., Caricato, M., Marenich, A.
915 V., Bloino, J., Janesko, B. G., Gomperts, R., Mennucci, B., Hratchian, H. P., Ortiz, J. V.,
916 Izmaylov, A. F., Sonnenberg, J. L., Williams-Young, D., Ding, F., Lipparini, F., Egidi, F.,
917 Goings, J., Peng, B., Petrone, A., Henderson, T., Ranasinghe, D., Zakrzewski, V. G., Gao, J.,
918 Rega, N., Zheng, G., Liang, W., Hada, M., Ehara, M., Toyota, K., Fukuda, R., Hasegawa, J.,
919 Ishida, M., Nakajima, T., Honda, Y., Kitao, O., Nakai, H., Vreven, T., Throssell, K.,
920 Montgomery, J. A., Peralta, J. J. E., Ogliaro, F., Bearpark, M. J., Heyd, J. J., Brothers, E. N.,
921 Kudin, K. N., Staroverov, V. N., Keith, T. A., Kobayashi, R., Normand, J., Raghavachari, K.,
922 Rendell, A. P., Burant, J. C., Iyengar, S. S., Tomasi, J., Cossi, M., Millam, J. M., Klene, M.,
923 Adamo, C., Cammi, R., Ochterski, J. W., Martin, R. L., Morokuma, K., Farkas, O., Foresman,
924 J. B., and Fox, D. J.: Gaussian 16, Revision B.01, Gaussian, Inc., Wallingford CT, 2016.

925 Fu, Z., Guo, S., Xie, H. B., Zhou, P., Boy, M., Yao, M., and Hu, M.: A near-explicit reaction
926 mechanism of chlorine-initiated limonene: implications for health risks associated with the
927 concurrent use of cleaning agents and disinfectants, *Environ. Sci. Technol.*, 58, 19762-19773,
928 <https://doi.org/10.1021/acs.est.4c04388>, 2024.

929 Fu, Z., Ma, F., Liu, Y., Yan, C., Huang, D., Chen, J., Elm, J., Li, Y., Ding, A., Pichelstorfer, L., Xie,
930 H. B., Nie, W., Francisco, J. S., and Zhou, P.: An overlooked oxidation mechanism of toluene:
931 computational predictions and experimental validations, *Chem. Sci.*, 14, 13050-13059,
932 <https://doi.org/10.1039/D3SC03638C>, 2023.

933 Fu, Z., Xie, H. B., Elm, J., Guo, X., Fu, Z., and Chen, J.: Formation of low-volatile products and
934 unexpected high formaldehyde yield from the atmospheric oxidation of methylsiloxanes,
935 *Environ. Sci. Technol.*, 54, 7136-7145, <https://doi.org/10.1021/acs.est.0c01090>, 2020.

936 Fukui, K.: The path of chemical reactions - the IRC approach, *Acc. Chem. Res.*, 14, 363-368,
937 <https://doi.org/10.1021/ar00072a001>, 1981.

938 Garmash, O., Rissanen, M. P., Pullinen, I., Schmitt, S., Kausiala, O., Tillmann, R., Zhao, D.,
939 Percival, C., Bannan, T. J., Priestley, M., Hallquist, Å M., Kleist, E., Kiendler-Scharr, A.,
940 Hallquist, M., Berndt, T., McFiggans, G., Wildt, J., Mentel, T. F., and Ehn, M.:
941 Multi-generation OH oxidation as a source for highly oxygenated organic molecules from
942 aromatics, *Atmos. Chem. Phys.*, 20, 515-537, <https://doi.org/10.5194/acp-20-515-2020>, 2020.

943 Gilbert, R. G., and Smith, S. C.: *Theory of unimolecular and recombination reactions*, Blackwell
944 Scientific: Carlton, Australia, 1990.

945 Glowacki, D. R., Liang, C. H., Morley, C., Pilling, M. J., and Robertson, S. H.: MESMER: an
946 open-source master equation solver for multi-energy well reactions, *J. Phys. Chem. A*, 116,
947 9545-9560, <https://doi.org/10.1021/jp3051033>, 2012.

948 Holbrook, K. A., Pilling, M. J., Robertson, S. H., and Robinson, P. J.: *Unimolecular reactions*, 2nd
949 ed.; Wiley: New York, 1996.

950 Huang, Y., Su, T., Wang, L., Wang, N., Xue, Y., Dai, W., Lee, S. C., Cao, J., and Ho, S. S. H.:
951 Evaluation and characterization of volatile air toxics indoors in a heavy polluted city of
952 northwestern China in wintertime, *Sci. Total Environ.*, 662, 470-480,
953 <https://doi.org/10.1016/j.scitotenv.2019.01.250>, 2019.

954 Iuga, C., Galano, A., and Vivier-Bunge, A.: Theoretical investigation of the OH-initiated oxidation
955 of benzaldehyde in the troposphere, *Chem. Phys. Chem.*, 9, 1453-1459,
956 <https://doi.org/10.1002/cphc.200800144>, 2008.

957 Iyer, S., Kumar, A., Savolainen, A., Barua, S., Daub, C., Pichelstorfer, L., Roldin, P., Garmash, O.,
958 Seal, P., Kurtén, T., and Rissanen, M.: Molecular rearrangement of bicyclic peroxy radicals is
959 a key route to aerosol from aromatics, *Nat. Commun.*, 14, 4984-4991,
960 <https://doi.org/10.1038/s41467-023-40675-2>, 2023.

961 Ji, Y., Zhao, J., Terazono, H., Misawa, K., Levitt, N. P., Li, Y., Lin, Y., Peng, J., Wang, Y., Duan, L.,
962 Pan, B., Zhang, F., Feng, X., An, T., Marrero-Ortiz, W., Secret, J., Zhang, A. L., Shibuya, K.,
963 Molina, M. J., and Zhang, R.: Reassessing the atmospheric oxidation mechanism of toluene,
964 *Proc. Natl. Acad. Sci. U.S.A.*, 114, 8169-8174, <https://doi.org/10.1073/pnas.1705463114>,
965 2017.

966 Koppmann, R.: *Volatile organic compounds in the atmosphere*, John Wiley & Sons, 2008.

967 Li, M., Zhang, Q., Zheng, B., Tong, D., Lei, Y., Liu, F., Hong, C., Kang, S., Yan, L., Zhang, Y., Bo,
968 Y., Su, H., Cheng, Y., and He, K.: Persistent growth of anthropogenic non-methane volatile
969 organic compound (NMVOC) emissions in China during 1990-2017: drivers, speciation and
970 ozone formation potential, *Atmos. Chem. Phys.*, 19, 8897-8913,
971 <https://doi.org/10.5194/acp-19-8897-2019>, 2019.

972 Lu, T.: Molclus program, Version 1.9.3. <http://www.keinsci.com/research/molclus.html> (accessed
973 May 21, 2024).

974 Ma, F., Guo, X., Xia, D., Xie, H. B., Wang, Y., Elm, J., Chen, J., and Niu, J.: Atmospheric
975 chemistry of allylic radicals from isoprene: a successive cyclization-driven autoxidation
976 mechanism, *Environ. Sci. Technol.*, 55, 4399-4409, <https://doi.org/10.1021/acs.est.0c07925>,
977 2021.

978 Møller, K. H., Berndt, T., and Kjaergaard, H. G.: Atmospheric autoxidation of amines, *Environ.*
979 *Sci. Technol.*, 54, 11087-11099, <https://doi.org/10.1021/acs.est.0c03937>, 2020.

980 Møller, K. H., Otkjær, R. V., Hyttinen, N., Kurtén, T., and Kjaergaard, H. G.: Cost-effective
981 implementation of multiconformer transition state theory for peroxy radical hydrogen shift
982 reactions, *J. Phys. Chem. A*, 120, 10072-10087, <https://doi.org/10.1021/acs.jpca.6b09370>,
983 2016.

984 Molteni, U., Bianchi, F., Klein, F., Haddad, I. E., Frege, C., Rossi, M. J., Dommen, J., and
985 Baltensperger, U.: Formation of highly oxygenated organic molecules from aromatic
986 compounds, *Atmos. Chem. Phys.*, 18, 1909-1921, <https://doi.org/10.5194/acp-18-1909-2018>,
987 2018.

988 Neese, F.: Software update: the ORCA program system—version 6.0, *Wires Comput. Mol. Sci.*, 15,
989 e70019, <https://doi.org/10.1002/wcms.70019>, 2025.

990 Nie, W., Yan, C., Huang, D. D., Wang, Z., Liu, Y., Qiao, X., Guo, Y., Tian, L., Zheng, P., Xu, Z., Li,
991 Y., Xu, Z., Qi, X., Sun, P., Wang, J., Zheng, F., Li, X., Yin, R., Dallenbach, K. R., Bianchi, F.,
992 Petäjä T., Zhang, Y., Wang, M., Schervish, M., Wang, S., Qiao, L., Wang, Q., Zhou, M.,
993 Wang, H., Yu, C., Yao, D., Guo, H., Ye, P., Lee, S., Li, Y. J., Liu, Y., Chi, X., Kerminen, V. M.,
994 Ehn, M., Donahue, N. M., Wang, T., Huang, C., Kulmala, M., Worsnop, D., Jiang, J., and
995 Ding, A.: Secondary organic aerosol formed by condensing anthropogenic vapours over
996 China's megacities, *Nat. Geosci.*, 15, 255-261, <https://doi.org/10.1038/s41561-022-00922-5>,
997 2022.

998 Orlando, J. J., and Tyndall, G. S.: Laboratory studies of organic peroxy radical chemistry: an
999 overview with emphasis on recent issues of atmospheric significance, *Chem. Soc. Rev.*, 41,
1000 6294-6317, <https://doi.org/10.1039/C2CS35166H>, 2012.

1001 Pankow, J. F., and Asher, W. E.: SIMPOL.1: a simple group contribution method for predicting
1002 vapor pressures and enthalpies of vaporization of multifunctional organic compounds, *Atmos.*
1003 *Chem. Phys.*, 8, 2773-2796, <https://doi.org/10.5194/acp-8-2773-2008>, 2008.

1004 Pasik, D., Frandsen, B. N., Meder, M., Iyer, S., Kurtén, T., and Myllys, N.: Gas-phase oxidation of
1005 atmospherically relevant unsaturated hydrocarbons by acyl peroxy radicals, *J. Am. Chem.*
1006 *Soc.*, 146, 13427-13437, <https://doi.org/10.1021/jacs.4c02523>, 2024.

1007 Sebbar, N., Bozzelli, J. W., and Bockhorn, H.: Thermochemistry and reaction paths in the
1008 oxidation reaction of benzoyl radical: C₆H₅C(=O), *J. Phys. Chem. A*, 115, 11897-11914,
1009 <https://doi.org/10.1021/jp2078067>, 2011.

1010 Shen, H., Vereecken, L., Kang, S., Pullinen, I., Fuchs, H., Zhao, D., and Mentel, T. F.: Unexpected
1011 significance of a minor reaction pathway in daytime formation of biogenic highly oxygenated
1012 organic compounds, *Sci. Adv.*, 8, eabp8702, <https://doi.org/10.1126/sciadv.abp8702>, 2022.

1013 Sun, J., Wu, F., Hu, B., Tang, G., Zhang, J., and Wang, Y.: VOC characteristics, emissions and
1014 contributions to SOA formation during hazy episodes, *Atmos. Environ.*, 141, 560-570,
1015 <https://doi.org/10.1016/j.atmosenv.2016.06.060>, 2016.

1016 Tajuelo, M., Bravo, I., Rodríguez, A., Aranda, A., D'áz-de-Mera, Y., and Rodríguez, D.:
1017 Atmospheric sink of styrene, α -methylstyrene, trans- β -methylstyrene and indene: Rate
1018 constants and mechanisms of Cl atom-initiated degradation, *Atmos. Environ.*, 200, 78-89,
1019 <https://doi.org/10.1016/j.atmosenv.2018.11.059>, 2019c.

1020 Tajuelo, M., Rodríguez, A., Baeza-Romero, M. T., Aranda, A., D'áz-de-Mera, Y., and Rodríguez,
1021 D.: Secondary organic aerosol formation from α -methylstyrene atmospheric degradation:
1022 Role of NO_x level, relative humidity and inorganic seed aerosol, *Atmos. Res.*, 230,
1023 104631-104640, <https://doi.org/10.1016/j.atmosres.2019.104631>, 2019b.

1024 Tajuelo, M., Rodríguez, D., Baeza-Romero, M. T., Díez-de-Mera, Y., Aranda, A., and Rodríguez,
1025 A.: Secondary organic aerosol formation from styrene photolysis and photooxidation with
1026 hydroxyl radicals, *Chemosphere*, 231, 276-286,
1027 <https://doi.org/10.1016/j.chemosphere.2019.05.136>, 2019a.

1028 Vereecken, L., Glowacki, D. R., and Pilling, M. J.: Theoretical chemical kinetics in tropospheric
1029 chemistry: methodologies and applications, *Chem. Rev.*, 115, 4063-4114,
1030 <https://doi.org/10.1021/cr500488p>, 2015.

1031 Wang, H., Ji, Y., Gao, Y., Li, G., and An, T.: Theoretical model on the formation possibility of
1032 secondary organic aerosol from OH initiated oxidation reaction of styrene in the presence of
1033 O₂/NO, *Atmos. Environ.*, 101, 1-9, <https://doi.org/10.1016/j.atmosenv.2014.10.042>, 2015.

1034 Wang, L., Wu, R., and Xu, C.: Atmospheric oxidation mechanism of benzene. Fates of alkoxy
1035 radical intermediates and revised mechanism, *J. Phys. Chem. A*, 117, 14163-14168,
1036 <https://doi.org/10.1021/jp4101762>, 2013.

1037 Wang, M., Chen, D., Xiao, M., Ye, Q., Stolzenburg, D., Hofbauer, V., Ye, P., Vogel, A. L., Mauldin,
1038 R. L., Amorim, A., Baccharini, A., Baumgartner, B., Brilke, S., Dada, L., Dias, A., Duplissy, J.,
1039 Finkenzeller, H., Garmash, O., He, X. C., Hoyle, C. R., Kim, C., Kvashnin, A., Lehtipalo, K.,
1040 Fischer, L., Molteni, U., Petřáková T., Pospisilova, V., Quémener, L. L. J., Rissanen, M., Simon,
1041 M., Tauber, C., Tomé A., Wagner, A. C., Weitz, L., Volkamer, R., Winkler, P. M., Kirkby, J.,
1042 Worsnop, D. R., Kulmala, M., Baltensperger, U., Dommen, J., El-Haddad, I., and Donahue,
1043 N. M.: Photo-oxidation of aromatic hydrocarbons produces low-volatility organic compounds,
1044 *Environ. Sci. Technol.*, 54, 7911-7921, <https://doi.org/10.1021/acs.est.0c02100>, 2020.

1045 Wang, S., and Li, H.: NO₃-initiated gas-phase formation of nitrated phenolic compounds in
1046 polluted atmosphere, *Environ. Sci. Technol.*, 55, 2899-2907,
1047 <https://doi.org/10.1021/acs.est.0c08041>, 2021.

1048 Wang, S., Newland, M. J., Deng, W., Rickard, A. R., Hamilton, J. F., Muñoz, A., Ródenas, M.,
1049 Vázquez, M. M., Wang, L., and Wang, X.: Aromatic photo-oxidation, a new source of
1050 atmospheric acidity, *Environ. Sci. Technol.*, 54, 7798-7806,
1051 <https://doi.org/10.1021/acs.est.0c00526>, 2020.

1052 Wang, S., Wu, R., Berndt, T., Ehn, M., and Wang, L.: Formation of highly oxidized radicals and
1053 multifunctional products from the atmospheric oxidation of alkylbenzene, *Environ. Sci.*
1054 *Technol.*, 51, 8442-8449, <https://doi.org/10.1021/acs.est.7b02374>, 2017.

1055 Wu, R., Pan, S., Li, Y., and Wang, L.: Atmospheric oxidation mechanism of toluene, *J. Phys.*
1056 *Chem. A*, 118, 4533-4547, <https://doi.org/10.1021/jp500077f>, 2014.

1057 Wu, X., Hou, Q., Huang, J., Chai, J., and Zhang, F.: Exploring the OH-initiated reactions of
1058 styrene in the atmosphere and the role of van der Waals complex, *Chemosphere*, 282,
1059 131004-131012, <https://doi.org/10.1016/j.chemosphere.2021.131004>, 2021.

1060 Wu, X., Huang, C., Niu, S., and Zhang, F.: New theoretical insights into the reaction kinetics of
1061 toluene and hydroxyl radicals, *Phys. Chem. Chem. Phys.*, 22, 22279-22288,
1062 <https://doi.org/10.1039/D0CP02984J>, 2020.

1063 Xu, L., Møller, K. H., Crouse, J. D., Kjaergaard, H. G., and Wennberg, P. O.: New insights into
1064 the radical chemistry and product distribution in the OH-initiated oxidation of benzene,
1065 *Environ. Sci. Technol.*, 54, 13467-13477, <https://doi.org/10.1021/acs.est.0c04780>, 2020.

1066 Yan, Y., Cabrera-Perez, D., Lin, J., Pozzer, A., Hu, L., Millet, D. B., Porter, W. C., and Lelieveld,
1067 J.: Global tropospheric effects of aromatic chemistry with the SAPRC-11 mechanism

1068 implemented in GEOS-Chem version 9-02, *Geosci. Model Dev.*, 12, 111-130,
1069 <https://doi.org/10.5194/gmd-12-111-2019>, 2019.

1070 Yang, F., Deng, F., Pan, Y., Zhang, Y., Tang, C., and Huang, Z.: Kinetics of hydrogen abstraction
1071 and addition reactions of 3-hexene by OH radicals, *J. Phys. Chem. A*, 121, 1877-1889,
1072 <https://doi.org/10.1021/acs.jpca.6b11499>, 2017.

1073 Yu, S., Jia, L., Xu, Y., and Pan, Y.: Formation of extremely low-volatility organic compounds from
1074 styrene ozonolysis: Implication for nucleation, *Chemosphere*, 305, 135459-135467,
1075 <https://doi.org/10.1016/j.chemosphere.2022.135459>, 2022.

1076 Yu, S., Jia, L., Xu, Y., and Pan, Y.: Molecular composition of secondary organic aerosol from
1077 styrene under different NO_x and humidity conditions, *Atmos. Res.*, 266, 105950-10604,
1078 <https://doi.org/10.1016/j.atmosres.2021.105950>, 2022.

1079 Zaytsev, A., Koss, A. R., Breitenlechner, M., Krechmer, J. E., Nihill, K. J., Lim, C. Y., Rowe, J. C.,
1080 Cox, J. L., Moss, J., Roscioli, J. R., Canagaratna, M. R., Worsnop, D. R., Kroll, J. H., and
1081 Keutsch, F. N.: Mechanistic study of the formation of ring-retaining and ring-opening
1082 products from the oxidation of aromatic compounds under urban atmospheric conditions,
1083 *Atmos. Chem. Phys.*, 19, 15117-15129, <https://doi.org/10.5194/acp-19-15117-2019>, 2019.

1084 Zhang, H., Wang, J., Dong, B., Xu, F., Liu, H., Zhang, Q., Zong, W., and Shi, X.: New mechanism
1085 for the participation of aromatic oxidation products in atmospheric nucleation, *Sci. Total*
1086 *Environ.*, 917, 170487-170494, <https://doi.org/10.1016/j.scitotenv.2024.170487>, 2024.

1087 Zhang, R. M., Truhlar, D. G., and Xu, X.: Kinetics of the toluene reaction with OH radical,
1088 *Research*, 2019, Article ID 5373785, <https://doi.org/10.34133/2019/5373785>, 2019.

1089 Zhao, H., Zhang, Y., Zhao, Q., Li, Y., and Huang, Z.: A theoretical study of H-abstractions of
1090 benzaldehyde by H, O³(P), ³O₂, OH, HO₂, and CH₃ radicals: Ab initio rate coefficients and
1091 their uncertainty quantification, *J. Phys. Chem. A*, 126, 7523-7533,
1092 <https://doi.org/10.1021/acs.jpca.2c02384>, 2022.

1093 Zhao, Y., and Truhlar, D. G.: The M06 suite of density functionals for main group
1094 thermochemistry, thermochemical kinetics, noncovalent interactions, excited states, and
1095 transition elements: two new functionals and systematic testing of four M06-class functionals
1096 and 12 other functionals, *Theor. Chem. Acc.*, 120, 215-241,
1097 <https://doi.org/10.1007/s00214-007-0310-x>, 2008.

1098